# Role of Clouds in the Urban Heat Island and Extreme Heat: Houston-Galveston Metropolitan Area Case.

John F. Mejia[1] https://orcid.org/0000-0001-6727-5541

Juan Jose Henao[1] https://orcid.org/0000-0002-1141-7683

Ebrahim Eslami[2] https://orcid.org/0000-0002-7721-6534

**1. Division of Atmospheric Sciences, Desert Research Institute, Reno, Nevada.**

**2. Houston Advance Research Center, The Woodlands, Texas.**

Corresponding author: John F. Mejia (john.mejia@dri.edu); 2215 Raggio Parkway, Reno, NV 89512.

**Key Points:**

- Urbanization correlates with the presence of shallow cumulus clouds.
- Urban clouds are driven by the enhanced sensible heat and dynamic drag imparted by the urban landscape.
- Urbanization cloud enhancement emerges as a crucial pathway responsible for reducing the afternoon Heat Index values.

## Abstract

The study and simulation of the Urban Heat Island (UHI) and Heat Index (HI) effects in the Houston-Galveston metropolitan area demand special attention, particularly in considering moist processes aloft. During the warm season, the afternoon sea breeze phenomenon in this coastal city acts as a natural air conditioner for city residents, facilitating the dispersion of moisture, heat, and pollutants. To delve into the intricate relationships among urbanization, clouds, and land-sea interactions, we conducted cloud- and urban-resolving simulations at a 900 m grid resolution. Results show that urbanization correlates with the presence of shallow cumulus clouds, higher cloud bases, and increased cloud duration over the Galveston-Houston region compared to rural areas. These urban clouds benefit from the enhanced sensible heat and dynamic drag imparted by the urban landscape, thereby intensifying vertical mixing and moisture flux convergence. This dynamic interplay uplifts heat and moisture convergence, contributing to the enhancement of moist static energy that sustains the additional urban convection. Interestingly, our findings suggest that urbanization augments the mean HI while mitigating its afternoon high. An urban circulation dome emerges, overpowering the influence of land-sea circulations. Contrary to expectations, urbanization doesn't seem to promote a stronger sea breeze that would favor moist and cooler air mass advection to the city. Instead, the influence of urbanization on cloud enhancement emerges as a crucial pathway responsible for reducing the afternoon HI values. Moreover, uncertainties in SSTs are closely linked to the sensitivities of land-sea circulations, which in turn modulate UHI and extreme heat indicators.



**Plain Language**

Urbanization influences the meteorology by creating a warmer environment that enhances excessive heat during the summer. Additionally, the warmer environment and the urban buildings increase friction, leading to more mixing and in turn favoring the development of low-level clouds. We developed computer simulations aiming to understand these processes and their interaction with the sea-breeze in this coastal city, and we found that these clouds help ameliorate the excessive heat during the afternoon.


Keywords: Urban clouds, Urban Heat Island, Urban Circulation, Sea Breeze, Heat Index.

# 1 Introduction

This study is motivated by the need to characterize and better simulate excessive heat in urban environments. Increasing population in urban areas make cities more vulnerable to extreme weather events, climate variations and warming trends. It is likely that some of these changes will be outside of the range of historical extremes (Simolo et al. 2011; Trenberth et al. 2015) and are expected to cause changes not only in mean, but also in extreme weather episodes (USGCRP, 2018). While there is relatively high confidence in the direction of changes in extreme temperature episodes, decision-makers require more quantitative and detail information to make better and more concrete adaptation plans to improve resilience in natural resources management (Rosenzweig et al. 2014) and health related risks (Guo et al. 2018; Ebi et al. 2021). The exposure of cities to extreme heat appears to be more critical under climate change scenarios and is exacerbated by the high solar absorption of the urban environments (i.e., the Urban Heat Island effect, hereafter UHI) (Fischer and Schär 2010; Schubert et al. 2012). Hence, understanding the processes modulating the extreme temperature is a necessary step to develop reliable adaptation and mitigations strategies aiming to make cities more resilient (Cady et al. 2020; Zonato et al. 2021; Resilient Houston 2020; Houston Climate Action Plan 2020).

Recent studies have found that the urban environments not only modulate the temperature via the UHI effect, but also clouds and precipitation (Loughner et al. 2011; Theeuwes et al. 2019; Fan et al. 2020; Doan et al. 2023; Vo et al. 2023; Statkewicz and Rappenglueck 2023). During the daytime, observations (Theeuwes et al. 2019), long-term satellite clouds retrievals (Vo et al. 2023) and numerical simulations (Loughner et al. 2011; Fan et al. 2020; Theeuwes et al. 2021) have shown that the urban environment enhance warm non-precipitating clouds (i.e., low-level shallow cumulus clouds) and even extreme precipitation (Fan et al. 2020; Doan et al. 2023).

During the night, however, Vo et al. (2023) suggested that clouds can block outgoing longwave radiation and exacerbate the UHI by suppressing the nighttime cooling.

The role of the urban environment on simulated warm non-precipitating low-level clouds needs a more systematic and deeper assessment as it can be influenced by the geography and climate of the region (Theeuwes et al. 2021; Vo et al. 2023; Chiu et al. 2022). For example, Vo et al. (2023) observed that urbanization in cities near the Gulf Coast tend to show larger cloud enhancements during the summer, compared to other regions in the continental United States. For a single storm event, Fan et al. (2020) simulated the individual and combined effects of the urban land-use/land-cover and aerosols on convective clouds, storm evolution and intensity. In agreement with Theeuwes et al. (2019, 2021), Fan et al. (2020) showed that Houston urban area is related to earlier occurring and more persistent clouds due to a stronger urban heating. They also showed that the aerosol-cloud interaction effect can develop deeper convective mixed-phase clouds and more intense storms as compared to the effect of the urban land-use/land-cover alone.

These cloud and precipitation enhancement favored by urbanization can modulate the UHI and extreme heat indicators. It is possible that the enhanced daytime clouds serve as a self-cooling mechanism by blocking the incoming solar radiation and increasing evaporative cooling. In coastal cities, however, isolating the effect of urbanization is challenging because the land-ocean sea breeze circulations can also invigorate clouds and precipitation (Loughner et al. 2011; Zhong et al. 2017) and overwhelm the signals related to urbanization, and other important processes such as aerosol-cloud interactions (Fan et al. 2020). During the extreme warm season, on the other hand, the relatively cold and moist air masses advected by the afternoon sea-breeze phenomenon provide a natural air conditioning to the city's residents, and facilitates the redistribution of pollutants, moisture, and heat.

93 The intricate interplay between Houston-Galveston urban morphology, local circulations,
94 and climate patterns significantly influences the formation and behavior of clouds over the city,
95 while their interactions with urban heat remain poorly understood. This study aims at
96 investigating the phenomenon of urban-induced clouds in the Houston region, elucidating the
97 underlying mechanisms driving their formation, encompassing both cloud dynamics and
98 thermodynamics mechanisms, and exploring their intricate relationship with surface temperature
99 and urban heat. To achieve this objective, we conducted urban-resolving and cloud-resolving
100 simulations (900 m grid size) using the Weather and Research Forecasting model (WRF; Powers
101 et al. 2017). Incorporating a multilayer Urban Canopy Model focused over the Houston-
102 Galveston area, our simulations leverage state-of-the-art representations of urban morphology
103 and Local Climate Zones (Demuzere et al. 2022). In Section 2, we describe the model
104 configuration, outline the observational data used for model evaluation, and elucidate the
105 rationale behind our experimental design, which aims to isolate the impacts of urbanization and
106 coastal influences. Moving forward to Section 3, we present the evaluation results of our model,
107 and examine the model representation of the UHI intensity, heat index, and shallow cumulus
108 clouds. Furthermore, we delve into the analysis of pertinent dynamical and thermodynamical
109 processes within the mixed layer, as well as the intricate land-sea interactions that drive cloud
110 enhancement. Finally, Section 5 offers a comprehensive discussion, reconciling new findings
111 and drawing conclusive insights from our study.

# 2 Data and Methodology

## 2.1 The Regional Climate Model Coupled with the Urban Canopy Model

We used the Weather Research and Forecasting model (WRFv4.3.2; Powers et al. 2017) configured to perform urban- and cloud-resolving simulations. For this, we implemented the urban canopy model (UCM) based on the multi-layer building effect parameterization (BEP) scheme, coupled with the Building Energy Model (BEM; Salamanca et al. 2010). This UCM option considers three-dimensional mass and momentum mixing and heat transfer between buildings and the atmosphere, providing a realistic and accurate representation of near-surface energy fluxes and air temperature in mid-latitude cities (Cady et al. 2020; Jin et al. 2021). We would like to stress that this is not an instance of model calibration, but an attempt to assess and understand the UCM's capabilities and related uncertainties. We used this UCM option, among others available, because it incorporates 11 Local Climate Zones (LCZ), with 10 built up categories that provide a better representation of the heterogeneity of urban areas as compared to the three built-up categories in other databases and UCMs.

In this study, we used a three nested domain configuration (8100 m, 2700 m, and 900 m) centered in Houston, with 61 vertical levels up to 100 hPa. To allow the innermost model domain to relax towards the scenario settings, we designed the borders to be at least 80 km away from the suburban areas of Houston. Our initial modeling tests showed significant numerical diffusion noise, highlighted as non-physical wind street patterns and thermal fields in the mixing layer with a spatial scale of two times the grid size. This problem is relatively common in high-resolution simulations during weak wind conditions and weak or unstable stratification (Knievel et al. 2007; Crosman et al. 2012). To overcome this issue, we imposed a spatial filter based on an explicit $6^{th}$-order numerical diffusion scheme with a non-dimensional rate of 0.12. Despite the potential over

smoothing in space of surface processes, the explicit diffusion treatment notably improved simulations, and results were resistant and unsensitive to its implementation. Additionally, we combined our experience and literature reports to determine other configurations and the selection of physical parameterizations implemented in our model. We acknowledge that it is difficult to find a model configuration that is superior under different flow regimes and for the large variety of geography and urbanization settings. For parameterization of moist processes, we used the Thompson double-moment microphysics, whereas convection and clouds parameterization are resolved explicitly in all our model domains, except for the coarser grid (8100 m) where we used the Kain–Fritsch scheme. Additionally, we used the Dudhia and Rapid Radiative Transfer Model (RRTM) as shortwave and longwave radiation schemes, respectively; Noah-Multiparameterization, Monin-Obukhov and Yonsei University (YSU) were selected for land-surface model, surface layer, and planetary boundary layer (PBL) schemes, respectively. YSU PBL scheme was used for its simplicity, low computational cost and recognized good performance (Hendricks et al. 2020). The first 6 hours of the simulations were not considered to allow for the model spin up. We used the GDAS/FNL (the Global Data Administration System/Final) re-analysis dataset (National Centers for Environmental Prediction et al., 2015; hereafter "FNL") as initial and boundary conditions data, with SST skin temperature updated as bottom boundary condition SSTs every 6 hours.

## 2.2 Land Use/Land Cover and Urban Characterization

An important consideration in urban canopy modeling is the characterization of the Land Use/Land Cover (LULC) and urban categories. Most LULC products rely on remote sensing surveys with urban classification that are either outdated, such as the National Urban Database and Portal Tool (NUDAPT; Ching et al. 2009), or lack details even in major urban composition

158 features, such as the World Urban Database and Access Portal Tools version 2 (WUDAPT;
159 Brousse et al. 2016; Ching et al. 2018; Demuzere et al. 2021, 2022a). Additionally, differences
160 in the algorithms used to characterize urban categories and different data sources may result in
161 different urban coverage. We opted to implement the 100 m global map of LCZ (Demuzere et al.
162 2022) for the following considerations: it follows the WUDAPT protocol; it is based on more
163 modern (2016-2018) data than NUDAPT (2006), thus it captures a more recent snapshot of the
164 urban growth and with a better spatial resolution; and their land cover classification adapted to
165 the LCZ and WUDAPT that facilitate their implementation of the UCM BEM+BEP for 11
166 different urban categories, contrasting only three urban categories in the NUDAPT data.
167 Recently, the global LCZ map was introduced into WRF preprocessing system (Demuzere et al.,
168 2023). However, we did not implement this version as the LCZ rely on urban pixels from other
169 databases (MODIS and Copernicus), producing a smaller urban area in comparison to the
170 original global LCZ map for the study region. The preprocessing for WRF was performed using
171 the WUDAPT-to-WRF (W2W) python tool (Demuzere et al., 2022b).

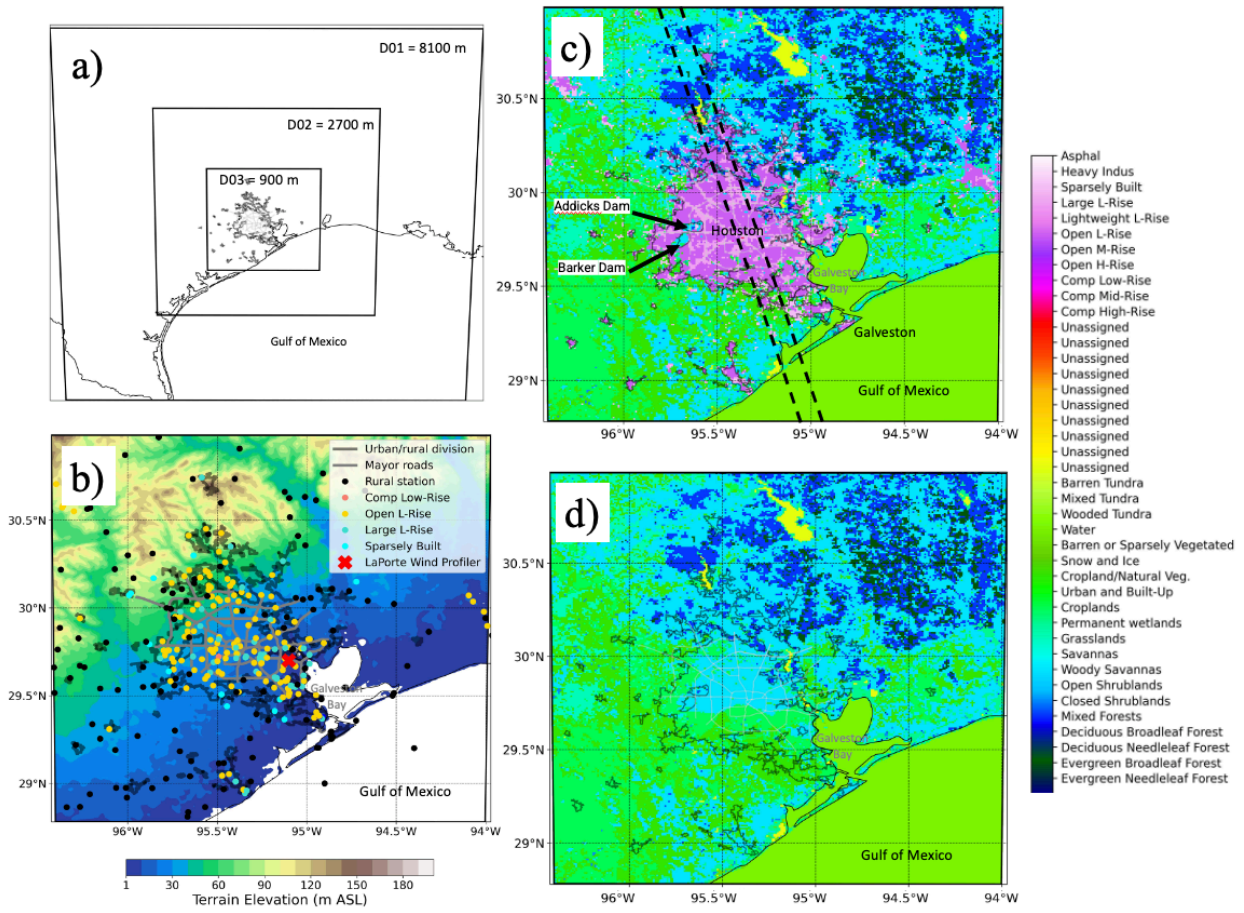


**Figure 1.** (a) WRF model nested domains (8000, 2700, 900 m grid sizes) and (b-d) details of the innermost model domain: (b) terrain elevation and the location of the NOAA LaPorte wind profiler site and the surface stations used in the model evaluation (from various sources), categorized by urban Local Climate Zones (LCZ; color coded symbols; 151 sites) or rural land cover (black symbols; 91 sites); (c) Land Use/Land Cover (LULC; contours) based on Demuzere et al. (2022) using LCZ categories for the urban areas and MODIS for rural areas; and (d) LULC after removing the urban areas and replacing them with the surrounding predominant rural vegetation. Dark grey contours indicate urbanization boundaries as of 2010 (Houston-Galveston Area Council, H-GAC; https://www.h-gac.com/Home) and light grey polygons show location of major intraurban roads. Dash lines in (c) show the location of the cross-city transect shown in the analysis.

## 2.3 Model Experiment Design

All simulations cover a 15-day period, between August 1 and 16, 2020, which was the warmest period of 2020, and normally the warmest period of the year (Palecki et al. 2021). We excluded the initial 6 hours due to model spin-up issues. During the simulation period, however, different meteorological regimes could have modulated sea-breeze related convection

invigoration: a pre-trough regime (1-3 August), followed by a post-trough regime (4-5 August), and then the Bermuda high anticyclone was more pronounced (5-16 August) (Wang et al. 2022; https://earth.nullschool.net/). To isolate the effect of these intermittent and scattered summer showers (mostly concentrated during August 1-3), we constrained our analyses to times without significant observed precipitation events (< 5 mm) in the Houston-Galveston area.

#### 2.3.1 SST Sensitivity

The city's proximity to the Gulf of Mexico and the complex coastal shape of Galveston Bay warrants a careful look at the SST data used by the model as bottom boundary conditions (Hawbecker and Knievel 2022). When comparing the default FNL SST fields used by the model against measurements from remotely sensed NOAA-SNPP VIIRS SST (available daily at 4 km grid size; several snapshots per day; Bouali and Ignatov 2014) and buoy datasets (https://www.ndbc.noaa.gov/), we found an average offshore cold bias of nearly -1 °C (SFig. 1). To improve the SST fields, we implemented a time-space Barnes interpolation approach with successive correction using a Gaussian weight function departing from the untreated FNL SSTs until optimizing the agreement between the interpolated function and the measurements (the unbiased SSTs; SFig. 1).

#### 2.3.2 Clouds, Urbanization and Weather Sensitivity

We conducted a series of simulations to elucidate the intricate interplay between synoptic, sea-breeze, and cloud effects alongside urbanization's influence on meteorology.

Firstly, we established a Baseline simulation incorporating the LCZ categories to mimic the urban landscape, using the unbiased SST as bottom boundary conditions (as outlined in Section 2.3.1), along with cloud and precipitation physics representations (microphysics and convection). Clouds and showers, partly driven by the afternoon sea-breeze, can significantly

impact the UHI effect (Morris et al., 2001). However, given the relatively short duration of our simulations (15 days) and the sporadic nature of moist processes aloft, we executed a clear sky simulation (hereafter referred to as 'Clear sky') by deactivating microphysics and convection in the model. This method assists in partially isolating the impact of clouds and showers on the Urban Heat Island (UHI) effect. However, fully disentangling the role of clouds in the UHI presents a challenge due to their potential influence on mesoscale circulations, such as sea breezes and urban-rural thermal-related flows, which are known to also affect the UHI phenomenon.

To assess uncertainties associated with SSTs, we performed a simulation utilizing the original (untreated or biased) FNL SSTs fields (hereafter referred to as 'Biased SSTs'). Additionally, we isolated the urbanization effects within mesoscale circulations by eliminating all urban areas from the domains (hereafter referred to as 'No City'), replacing all urban grid points with representative regional vegetation (Fig. 1d). A summary of the simulations conducted in this study, along with their respective descriptions and justifications, is provided in Table 1. Of note is that all references to the model simulation pertain to the Baseline scenario, unless explicitly stated otherwise.

**Table 1.** Description of model scenarios simulated in for this study.

| ***Scenario name*** | ***Description*** | ***Justification*** |
|---|---|---|
| ***Baseline*** | *All sky simulation including cloud and convective processes (moist processes) and bias correction of offshore SSTs (unbiased SSTs). Includes WUDAPT data.* | *Full physics simulation using outlined parameterizations and state-of-the-art LULC categories from LCZ. Systematic biases associated with offshore SSTs are removed.* |
| ***Clear Sky*** | *Same as Baseline but without clouds and moist convective processes.* | *Isolate the role of clouds and precipitation relative to Baseline.* |
| ***Biased SST*** | *Same as Baseline but using the untreated biased SSTs* | *Assess the sensitivity of Baseline to SST perturbations or refinements (e.g., bias corrections).* |
| ***No City*** | *Same as Baseline but replacing the urban LCZ categories with rural land cover* | *Isolate the role of the urbanization in the meteorology.* |

## 2.4 Surface Station and Upper-Air Winds

We utilized all available, quality-controlled surface station monitoring sites in the Houston area and surrounding rural regions. Data was retrieved using the Synoptic Data Application Programming Interface (API) using data from the National Weather Service, Remote Automated Weather Station, and Texas Commission on Environmental Quality (TCEQ) Continuous Ambient Monitoring Station (CAMS) network. After stringent quality assurance/quality control checks (e.g., removing outliers, visual inspection, addressing atypical diurnal cycles of temperature and relative humidity), a total of 208 stations were deemed reliable, with 151 situated in urban settings (110 in Open L-Rise, 12 Sparsely built, 28 in Large L-Rise, and 1 in Open H-Rise) and 91 in rural areas (Fig. 1b). It is acknowledged that certain uncertainties may exist due to urban network siting and sensor variability, some of which were mainly designed for air quality monitoring purposes (e.g., TCEQ sites).

These surface station observations significantly contributed to assessing the model confidence in representing the diurnal temperature, relative humidity, and wind behavior, while facilitating the analysis of derived parameters such as minimum temperature (Tmin), maximum temperature (Tmax), Urban Heat Island (UHI) effect (calculated as the difference between representative urban and rural sites), and Heat Index, based on the Rothfusz (1990) formulation utilizing temperature and relative humidity data. Model confidence was assessed through metrics including model bias, root-mean-square-error (RMSE), and Pearson correlation coefficient. In order to enable a comprehensive comparison between urban and rural sites, we employed a bootstrapping methodology with replacement. This approach was designed to assess the uncertainty surrounding the impact of proximity to the coast and the consequent land-sea interaction effects. The bootstrapped analysis included an almost equal distribution of stations

between coastal and inland locations relative to downtown Houston, situated approximately 75 km from the Gulf coast. Consequently, coastal sites were classified as being within a coastal area if their distance from the Gulf coast was less than 75 km, while inland sites were those located further away.

To assess the accuracy of simulated low-level winds, we compared them against observations from the Cooperative Agency Profilers wind profiler at La Porte (LPTTX), situated near the coast along the northern shores of Galveston Bay (Fig. 1b).

# 3 Results

## 3.1 Model Evaluation

Figure 2 shows the observed and simulated diurnal patterns of surface temperature, relative humidity, Heat Index, and zonal and meridional winds, corresponding to urban and rural sites in the domain. In general, the model adequately follows the diurnal median patterns for the evaluated parameters, but several biases are apparent, with the model showing a systematic low relative humidity bias (also exhibited in the water vapor mixing ratio, not shown) that is more intense during the afternoon and nighttime. The model surface temperature shows an in-phase diurnal evolution with a warm bias in the late afternoon and during the nighttime. Of note is that model nighttime temperature biases are even warmer in urban sites compared to rural sites. The amplitude of the diurnal cycle of the simulated HI exhibits a smaller magnitude compared to observational estimates, characterized by a warm bias during nighttime and a cold bias during daytime periods. These biases in HI stem from a concurrent warm bias in surface temperature during the day and a dry bias in relative humidity during the night. Notably, these HI biases are more pronounced over urban sites, where the dry bias is more discernable.

Fig. 2 shows that the diurnal distribution of the simulated zonal winds closely follows the observations, with shifting from relatively calm southeasterlies in the morning to stronger southwesterlies in the afternoon and nighttime. Part of the wind shifting feature is typically a result from the planetary boundary layer diurnal inertial oscillation (Blackadar 1957); albeit diurnal variability at this region can also be driven by the land-sea circulation. A striking surface circulation feature is that wind speeds are stronger over rural areas compared to urban areas (Fig. 2). This urban-rural wind speed differences are overemphasized by the model: the simulated winds show a slightly stronger southerly wind bias in urban sites, whereas it almost doubles the observed southerly wind in rural sites.

To further assess low-level wind patterns (< 3 km), data from the La Porte wind profiler (Fig. 3) were incorporated into our evaluation analysis. Both model simulations and observational data revealed a nocturnal wind acceleration, a phenomenon associated with the prevailing summertime Great Plains low-level Jet circulation, which extends towards the Gulf coast in eastern Texas (Pu and Dickinson, 2014). However, notable disparities emerged between the model and the observed conditions at La Porte. The model exhibited a more pronounced and enduring nocturnal maximum, suggesting a deeper intensity compared to the observed jet. This finding agrees with the results of Ngan et al. (2013), who identified analogous biases in model-generated low-level wind patterns and intensities across various land surface and planetary boundary layer (PBL) parameterizations. Although it is out of the scope of this study, an energy and momentum budget can help elucidate and shed more light on the origin of the existing stronger southerly low-level wind biases.

Urban stations (151) Rural stations (91)

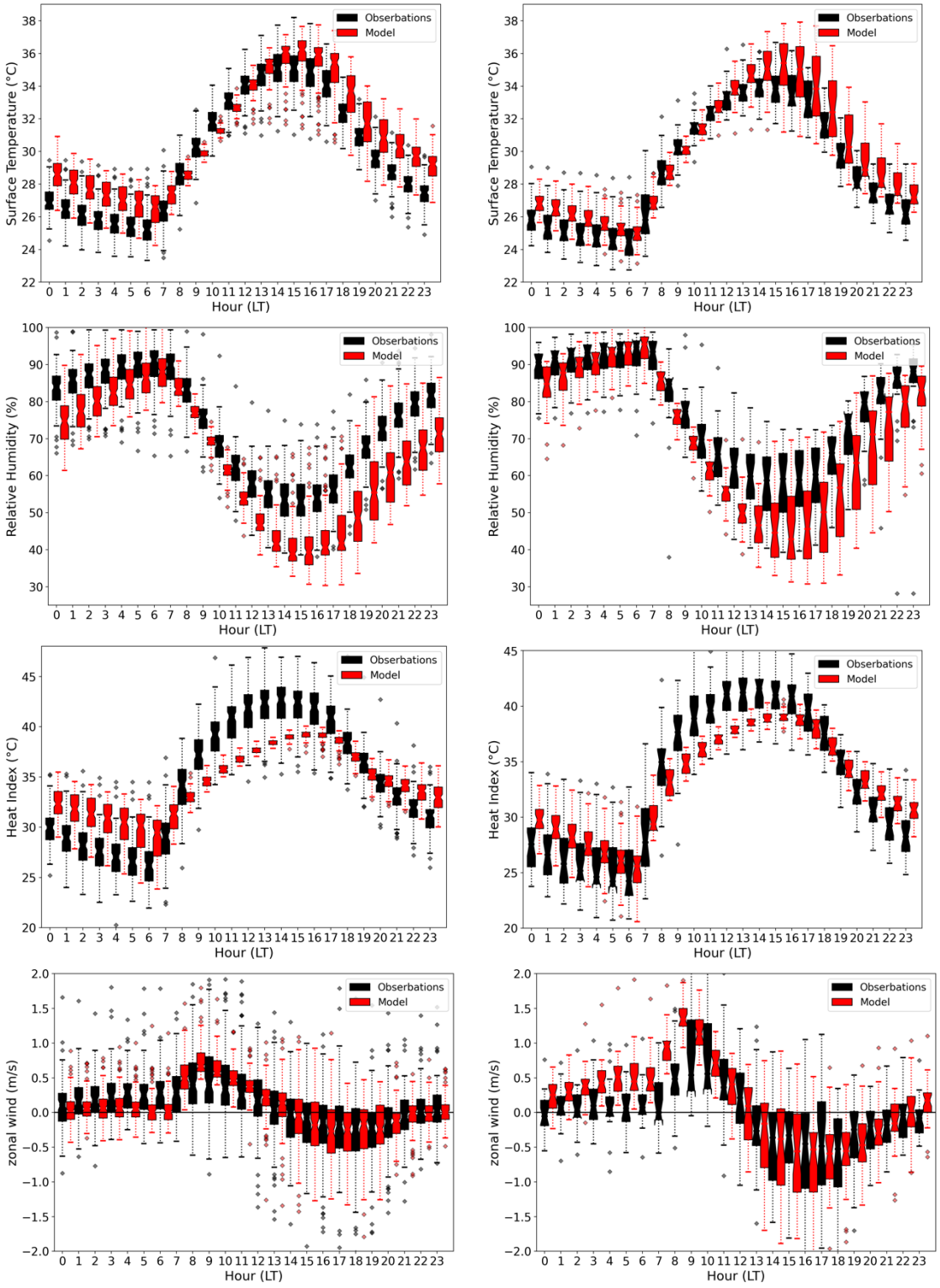
Surface Temperature (°C)
Relative Humidity (%)
Heat Index (°C)
zonal wind (m/s)
Hour (LT)
Obserbations
Model

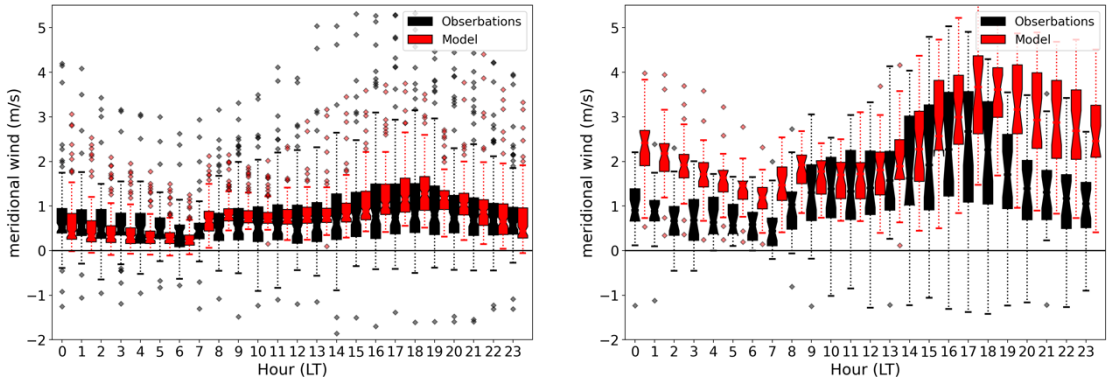


**Figure 2.** Baseline model and observed diurnal cycle distribution of (top to bottom panels) surface temperature, relative humidity, and zonal and meriodonal wind components for stations in the Houston urban (151 sites; left panels) and rural regions (91 sites; righ panels).

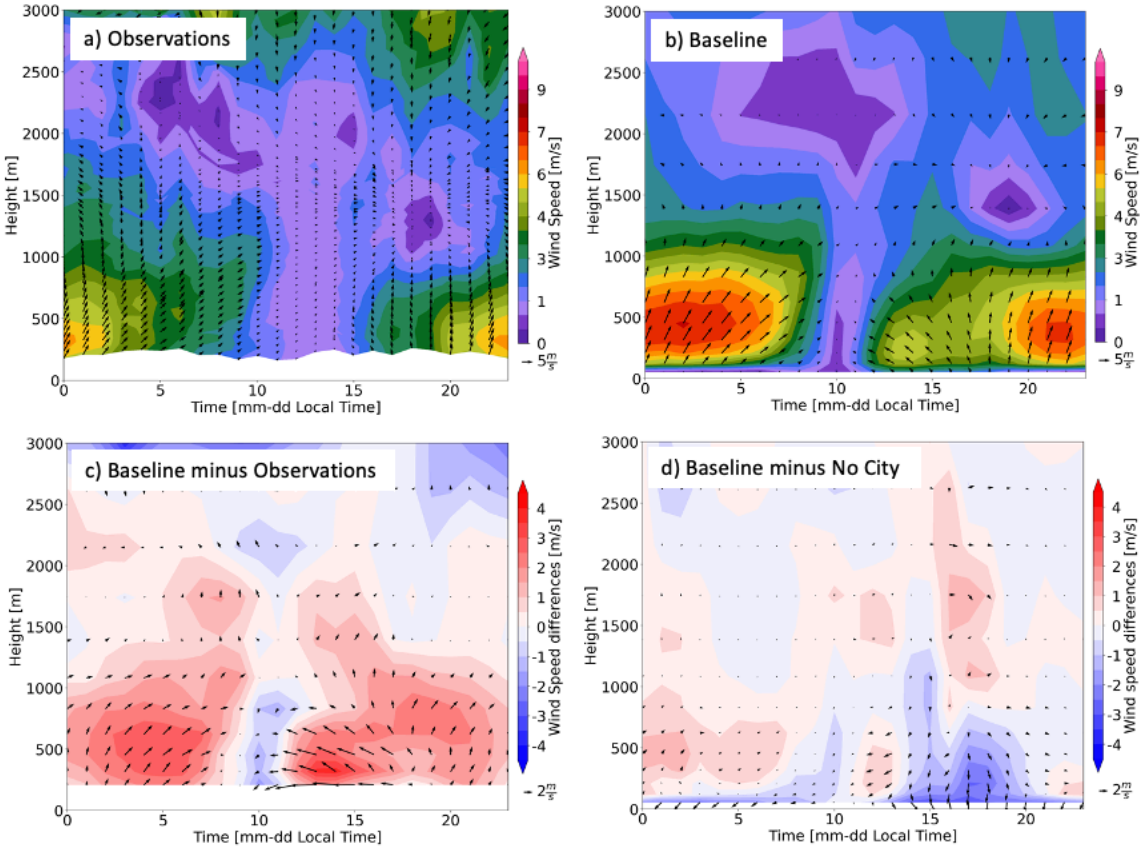


**Figure 3.** Low-level-diurnal mean horizontal wind speed (contours) and wind vectors (with the north direction pointing upwards) for (a) La Porte Wind profiler observations, (b) Baseline model winds, (c) Baseline minus observations differences and (d) Baseline minus No City differences.

Figure 4 shows the model scenarios biases (Table 1) for surface temperature and relative humidity, evaluated at all available surface station sites (see SFig. 2 for evaluation of the RMSE

and Pearson correlation coefficients). In general, model errors are small and well within the model typical behavior in perturbed sensitivity experiments (Ancell et al. 2018; Wang et al. 2023), but some systematic error signals emerged as a function of the scenario simulations and by compositing rural and urban areas. The Baseline simulation shows a systematic warm bias for Tmin and Tmax. Not surprisingly, over the urban areas the No City scenario shows a relatively colder bias when compared to all the urbanized scenarios.

The role of clouds in the model performance is apparent. Notably, the Clear sky scenario has warmer and drier biases during the daytime, as the lack of clouds increases the incoming solar radiation, balanced by more sensible and ground heating. At night, the warmer biases of the Clear sky scenario, as compared to Baseline biases, suggest that the outflux ground heating dominate the faster longwave radiation cooling (Fig. 5).

When comparing the Baseline to the Biased SSTs scenario, refining the offshore SSTs towards a warmer SSTs have an inland warming effect, with larger differences during early morning. Therein, a surprising result is that bias differences between Baseline and Biased SSTs are smaller during the daytime than during the early morning. This is related to the direct sea-breeze advection of warmer maritime surface temperature that does not develop a significant sensitivity in Tmax in comparison to Tmin. Therefore, the model biases highlight that the surface temperature sensitivity between the Baseline and Clear sky simulations (-0.56 °C difference) are significantly larger than that between the Baseline and Biased simulations (0.25 °C difference; see also SFig. 2). By construction, the bias trends of the scenarios in this model evaluation procedure are somehow expected, but some potential non-linear impacts related to changes in cloudiness and circulation, which motivate the main objective of this study, are not as apparent.

a) Surface temperature bias

b) Relative humidity bias

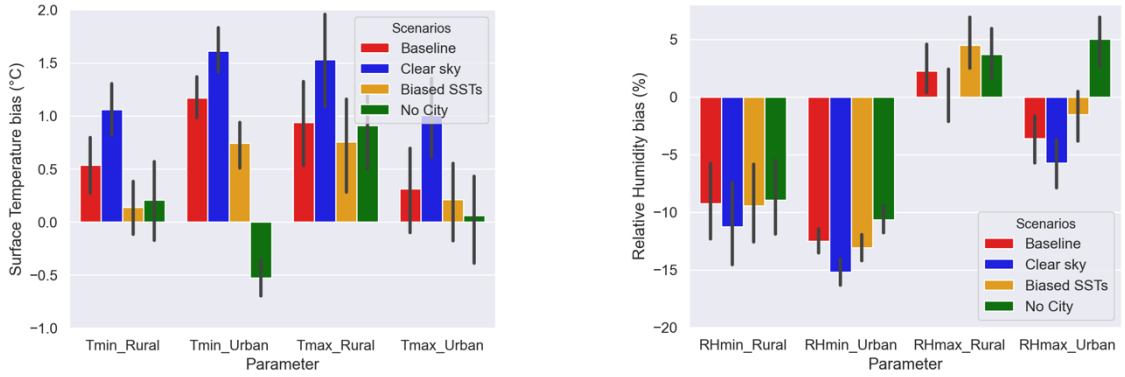


**Figure 4.** Model biases for each scenario (Table 1) evaluated at surface station sites for minimum and maximum (a) surface temperature and (b) relative humidity. Surface station sites are categorized as Urban or Rural according to land use/land cover types. Analysis is constrained to non-rainy periods as described in Section 2.

## 3.2 Urban Heat Island

Table 2 compares surface station observations and corresponding simulations composited as a function of the rural and urban categories. The UHI was estimated as the difference between the mean temperature of the stations in the urban and rural sites, determined for Tmax and Tmin. Since the distance from the coast (i.e., from the station to the nearest simulated ocean grid point) can have an impact in the UHI estimates (not shown), we used the median of the distance from the coast to subsample and balance the number of sites located near the coast with those far from the coast. Observations show a more pronounced UHI effect for Tmax (afternoon) than for Tmin (early morning). When contrasting the model at sites with surface station data, the Baseline model is overemphasizing the Tmin UHI effect and underemphasizing that of Tmax. Table 2 also shows that the Baseline simulation is related to a stronger Tmin and a milder Tmax UHI than the Clear sky scenario. This is not surprising due to the role of clouds in the long- and short-wave radiative balance (Brenguier et al. 2000). Biased SST simulation yields a similar and a more intense early morning and afternoon UHI, respectively. Finally, the relatively small

343 temperature differences in the No City simulation show that the composited UHI in the other
344 simulations are linked to urbanization.

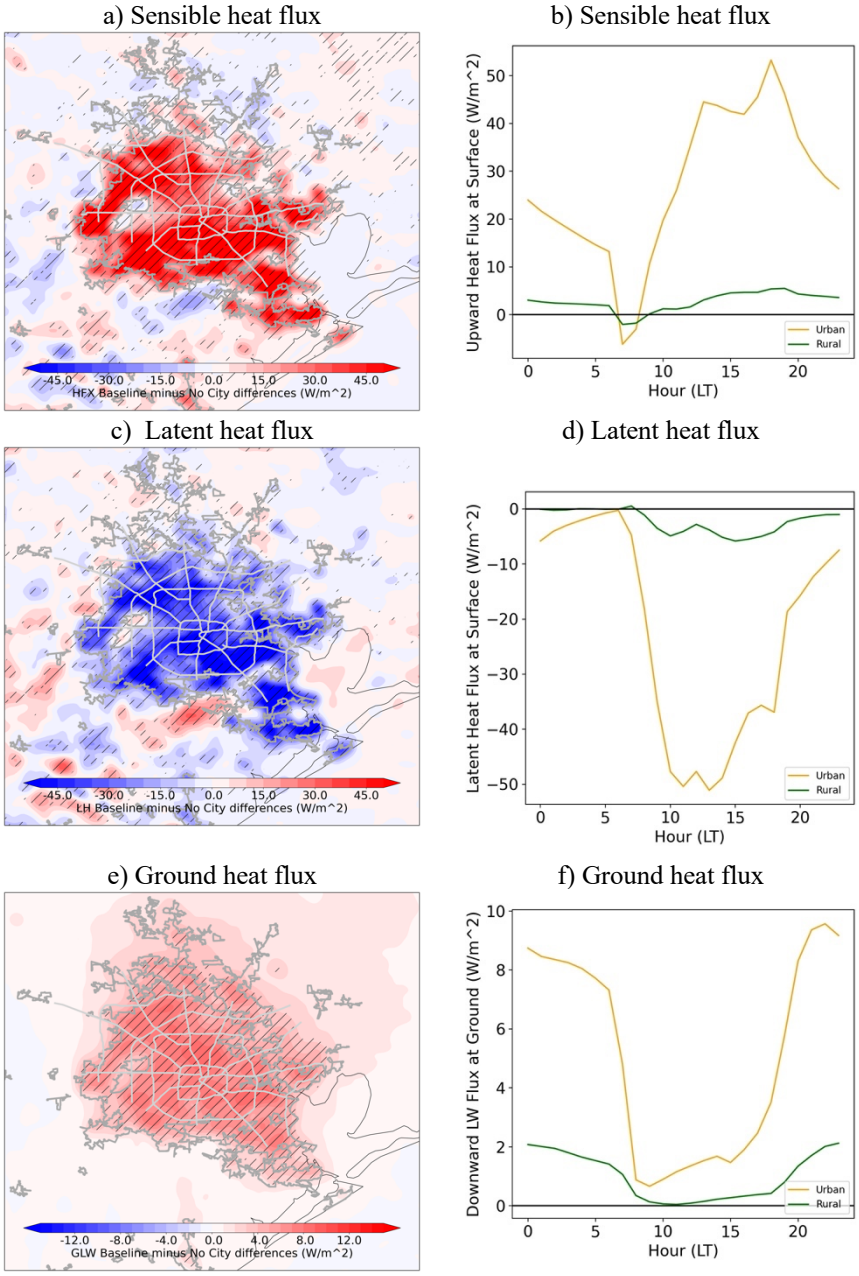


345 **Figure 5.** Mean Baseline minus No City differences for (a) sensible, (c) latent, (e) ground heat fluxes. Hatched areas
346 indicate that differences are significant with a 95% confidence level. Dark grey contours indicate urbanization
347 boundaries as of 2010 (Houston-Galveston Area Council, H-GAC; https://www.h-gac.com/Home) and light grey
348 show location of major intraurban highways. Spatially averaged diurnal (b) sensible, (d) latent and (f) ground heat
349 fluxes for Baseline minus No City differences composited by urban and rural areas.

Another method to reveal the intensity of the UHI is by comparing the Baseline and the No City scenarios. Fig. 6 shows the spatial patterns of the UHI effect for Tmin and Tmax, estimated as the Baseline minus the No City simulated differences. The nighttime and daytime UHI differences are striking, highlighting a very pronounced and significant early morning UHI effect and a less intense afternoon UHI effect (Fig. 6c). The urbanization intensity and intra-urban vegetation islands are related to some of the cool UHI patches within the city (Fig. 1c). Notably, the Baseline minus the No City differences remain significant downwind and to the north and northwest of the city boundary (Fig. 6). Since some stations are located downwind of Houston, this advection of UHI can reduce the actual UHI intensity estimates shown in Table 2. Hence, the overemphasis of the early morning (Tmin) UHI can be partly attributed to the overestimation of surface temperature in the urban areas.

**Table 2.** Observed and simulated (mean and bootstrapped 95% confidence interval using for 100 iterations with replacement) Tmin and Tmax at surface station locations composited by urban (117 sites) rural (91 sites) sites (see Fig. 1). The UHI effect is estimated as the urban minus rural difference for observations and each scenario, with bold estimates highlighting significant UHI effect with p-value of 0.05 and lower.

| | Tmin [°C] | | | | Tmax [°C] | | | | Tmin [°C] | | Tmax [°C] | |
|---|---|---|---|---|---|---|---|---|---|---|---|---|
| | Rural | | Urban | | Rural | | Urban | | UHI (Urban minus Rural) | | | |
| | Mean | C.I. 95% | Mean | C.I. 95% | Mean | C.I. 95% | Mean | C.I. 95% | Mean | p-value | Mean | pvalue |
| **Observations** | 24.56 | 0.28 | 25.18 | 0.19 | 34.52 | 0.24 | 35.65 | 0.22 | **0.62** | 0.0002 | **1.13** | P < 0.0001 |
| **Baseline** | 25.10 | 0.20 | 26.35 | 0.17 | 35.46 | 0.32 | 35.96 | 0.42 | **1.25** | <0.0001 | 0.50 | 0.0736 |
| **Clear sky-Baseline** | 25.62 | 0.19 | 26.80 | 0.17 | 36.05 | 0.34 | 36.65 | 0.41 | **1.18** | <0.0001 | **0.60** | 0.0358 |
| **Biased SSTs-Baseline** | 24.70 | 0.18 | 25.93 | 0.17 | 35.28 | 0.36 | 35.86 | 0.43 | **1.23** | <0.0001 | **0.58** | 0.0481 |
| **No City** | 24.77 | 0.18 | 24.66 | 0.09 | 35.43 | 0.34 | 35.71 | 0.47 | -0.11 | 0.2466 | 0.28 | 0.3668 |

## 3.3 The Role of Shallow Cumulus Clouds

Figures 7a and 7b show the mean vertical maximum cloud mixing ratio for the Baseline and No City scenarios, respectively. The Baseline urbanized area exhibits thicker and more abundant clouds compared to the "urban area" in the No City scenario, primarily attributed to afternoon shallow cumulus clouds (Fig. 7c). In contrast, the No City scenario shows a lower cloud cover with less apparent differences across the domain. The impact of urbanization on the cloud patterns is complex and can vary temporally and spatially. It is important to note that the patchy cloud structures are a result of the relatively short simulation, limiting a point-by-point

374 comparison between these scenarios. However, extending the model integration over a longer
375 duration is expected to reveal more robust and discernable differences. For instance, the cloud
376 frequency climatology by Wilson and Jetz (2016) unambiguously demonstrates that
377 urbanization-related clouds are more frequent than clouds in the surrounding rural areas. This
378 cloud climatology, developed at a 1 km grid size, further reveals intraurban variability in cloud
379 frequency, dependent on urbanization intensity and urban green infrastructures, as observed in
380 the less cloudy areas over the vegetated Addicks and Barker flood control reservoirs in the west
381 of Houston (Fig. 1c).

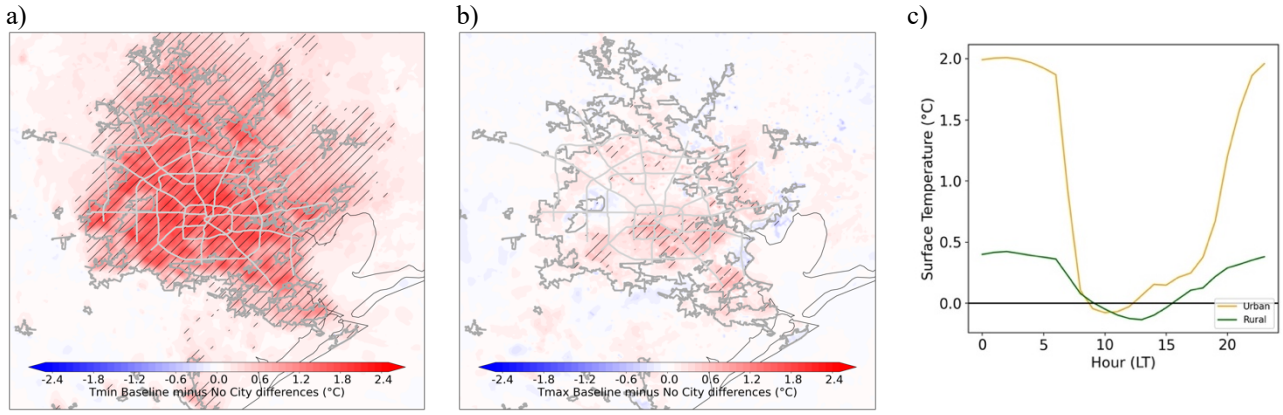


382 **Figure 6.** Mean Baseline minus No City differences for (a) Tmin and (b) Tmax. Hatched areas in (a) and (b)
383 indicate that differences are significant with a 95% confidence level. Dark grey contours indicate urbanization
384 boundaries as of 2010 (Houston-Galveston Area Council, H-GAC; https://www.h-gac.com/Home) and light grey
385 show location of major intraurban highways. (c) Spatially averaged diurnal surface temperature for Baseline minus
386 No City differences composited by urban and rural areas.

387 The impact of urbanization in the clouds is more apparent by averaging their properties in
388 space. Fig 8 presents the spatially averaged diurnal-pressure cloud mixing ratio for both the
389 Baseline and the No City scenarios, only considering urban grid points. In general, inland
390 shallow cumulus clouds begin forming early during the daytime, growing deeper and more
391 abundant around 15 LT. The Baseline simulation shows that these clouds are more abundant in
392 the urban areas than in the rural areas, while Baseline minus No City differences further confirm
393 that over built-up land cover these shallow cumuli are more abundant, grow deeper and last
394 longer than over vegetation. Although smaller differences are observed when comparing clouds
395 between the Baseline and No City scenarios in rural areas (not shown), some cloud mixing ratio

396 differences are simulated, likely due to the advection of UHI effects downstream into rural
397 regions (as shown for temperature in Fig. 6).

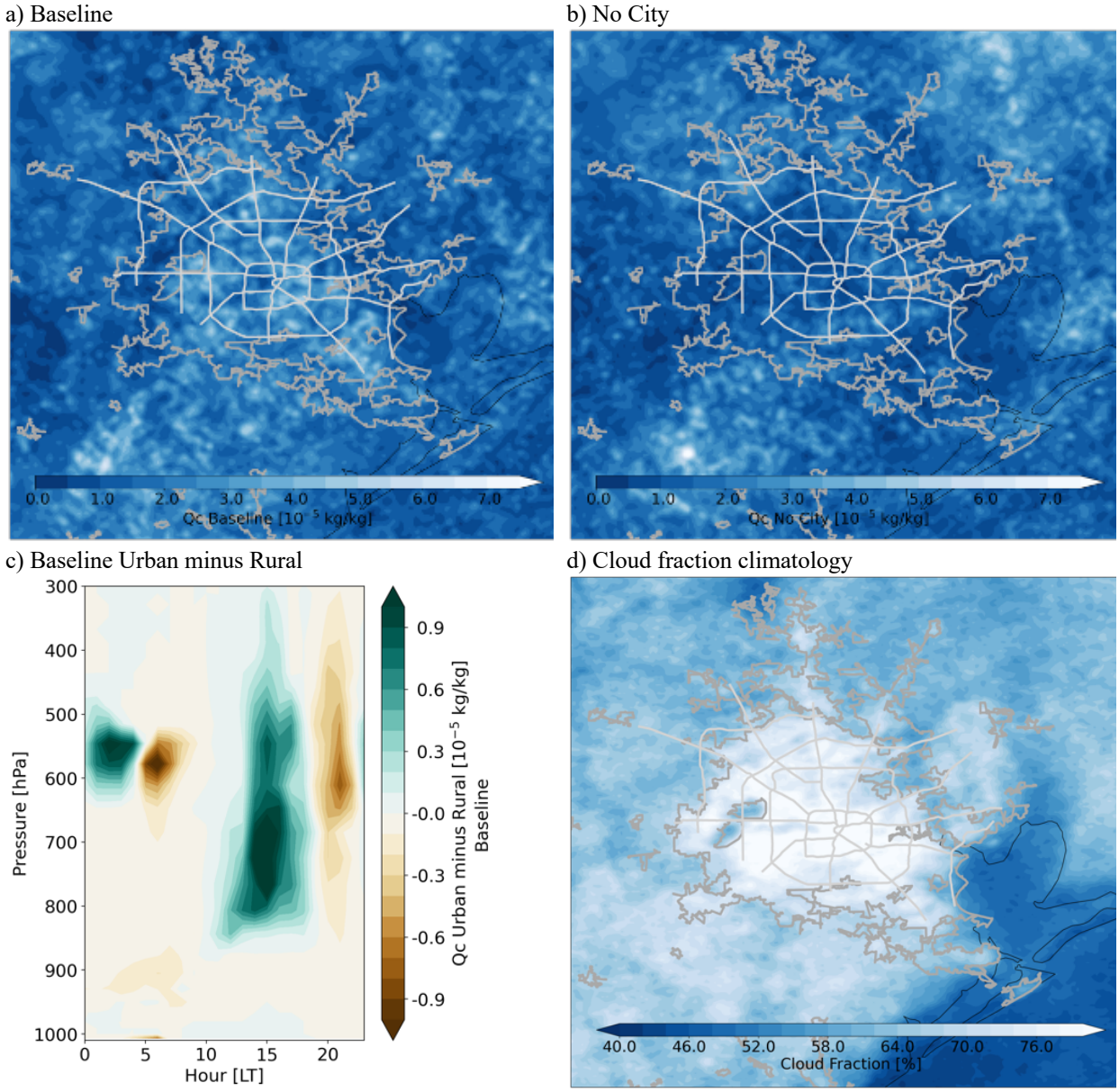


398 **Figure 7.** Mean vertical maximum cloud mixing ratio for (a) Baseline and (b) No City scenarios, and (c) Baseline
399 diurnal-pressure urban minus rural composites. (d) Cloud fraction climatology based on 15 years of twice-daily
400 Moderate Resolution Imaging Spectroradiometer (MODIS) satellite images (source Wilson and Jetz 2016). Dark
401 grey contours indicate urbanization boundaries as of 2010 (Houston-Galveston Area Council, H-GAC;
402 https://www.h-gac.com/Home) and light grey show location of major intraurban highways.
403

404

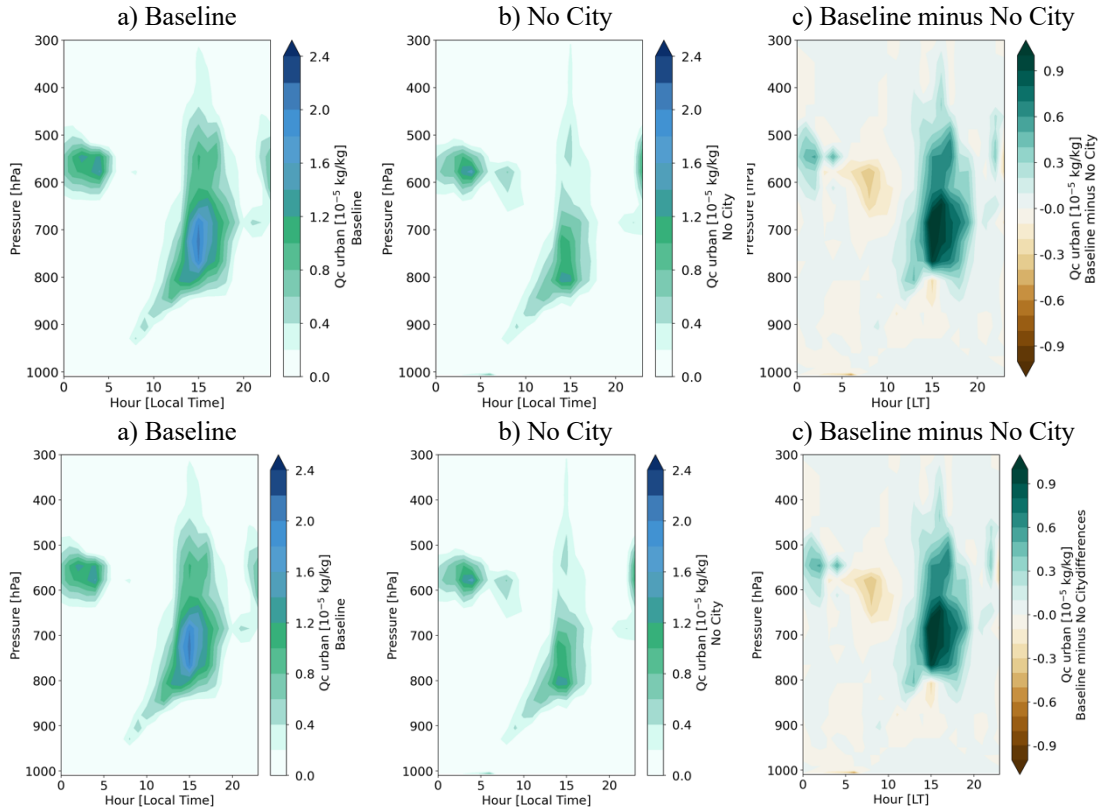


**Figure 8.** Diurnal-pressure mean urban cloud mixing ratio for a) Baseline, b) No City and c) Baseline minus No City scenarios differences. Urban grid points selected according to MODIS/WUDAPTv2 land use/land cover types.

Figure 9 shows that the cloud base is significantly higher and thicker in the urban mixing layer dome. Compared to the rural areas, an increase in cloud base height is expected in environments with lower relative humidity (Williams et al. 2015) or higher Bowen ratio (Chiu et al. 2022). Additionally, it is possible that the thicker mixed layer is favored by enhanced surface temperature, leading to enhanced sensible heat flux (Fig. 5), and by the apparent increase in urban aerodynamic roughness exhibited as a deceleration of the predominant south-southeasterly low-level wind over the urban area (Fig. 10). Notably, the urban PBL diurnal differences increase linearly after sunrise, but are damped around the time of maximum shallow cumulus (~15 LT), in which the enhanced clouds control a transient surface cooling effect and sensible heat flux reduction (Fig. 5), hence temporarily lowering the vertical mixing.

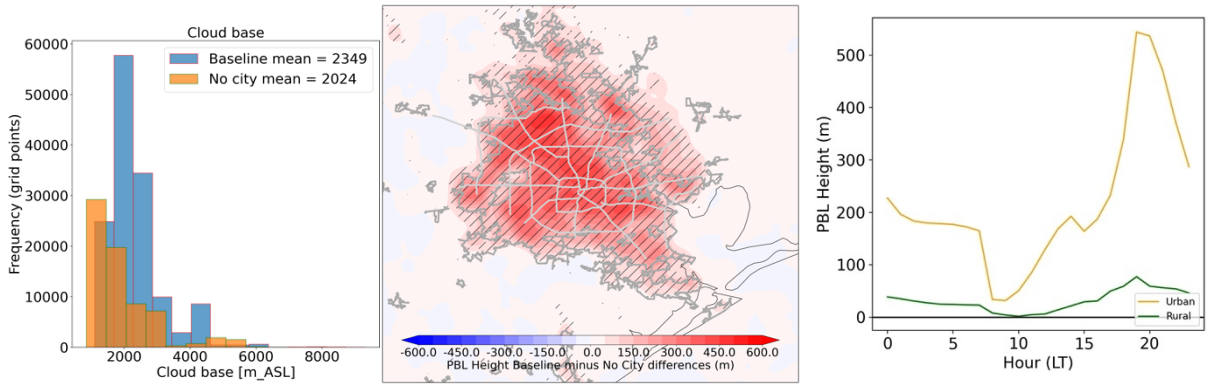


**Figure 9.** (Left panel) Cloud base distribution for the Baseline and No City scenarios over the urbanized area. Student's t-test and Kolmogorov–Smirnov test indicate that means and distributions are significantly different with 99% confidence level. (Middle panel) Baseline minus No City PBL height differences with hatched areas indicating that differences are significant with a 95% confidence level; Dark grey contours indicate urbanization boundaries as of 2010 (Houston-Galveston Area Council, H-GAC; https://www.h-gac.com/Home) and light grey show location of major intraurban highways. (Right panel) Baseline minus No City PBL height differences averaged over urban and rural areas.

To better understand the factors driving enhanced clouds over the urban dome, we examined the diurnal-height urbanization impacts for various dynamical and thermodyncamical parameters, using composites of the Baseline minus No City scenarios (Fig. 11). Synchronous with enhanced afternoon uplift, the urban dome extends up to ~2 km with a dipole of warmer and drier airmass over the city and cooler and moister air mass in the upper-mixing layer. A significant feature in Fig. 11 is that the mixed layer air entering the afternoon shallow cumulus clouds is related to enhanced Moist Static Energy (MSE), suggesting that the clouds convective updrafts (Fig. 11b) are dominated by the warmer temperature (Fig. 11a) and increased sensible heat flux near the surface, as well as enhanced water vapor in the upper-mixed layer (Fig. 11c). Dynamically, the enhanced water vapor air masses are sustained by the increases in both horizontal moisture flux convergence at low-levels and upward moisture flux convergence in the upper-mixed layer. Additionally, an urban-induced circulation cell with northerly low-level and south-southwesterly upper-mixed layer circulation disturbance (and enhanced moisture flux

439 divergence) is revealed. This circulation pattern in the urban dome resembles the self-contained
440 UHI circulation described by Fan et al. (2017). Moreover, Fig. 10 highlights the horizontal extent
441 of the low-level branch of this circulation, impacting beyond the urban area and well
442 downstream of the city.

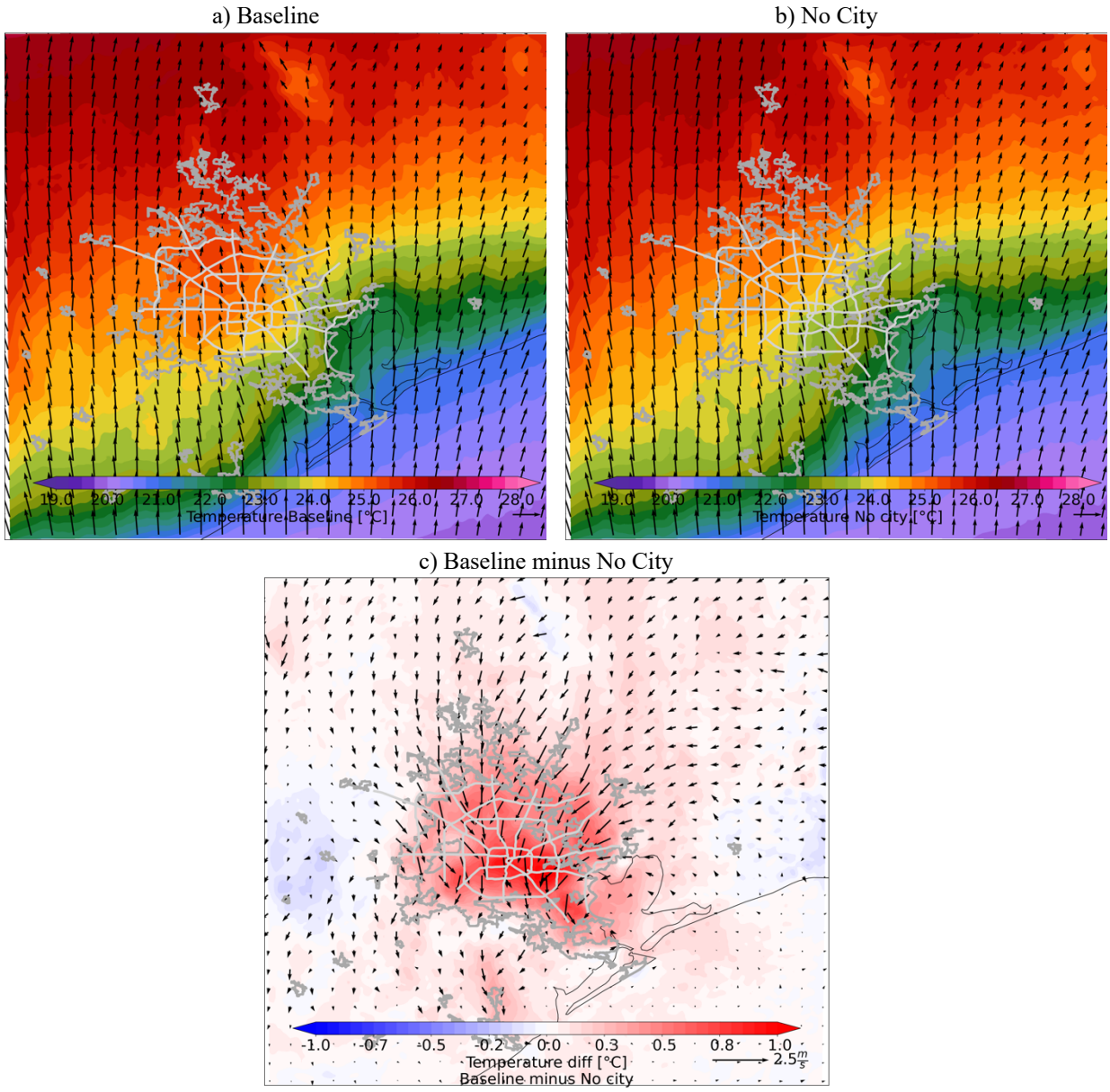


443 **Figure 10.** 500 m (above MSL) temperature and wind vectors for (a) Baseline, (b) No City and (c) Baseline minus
444 No City differences averaged between noon and 18 LTC. Dark grey contours indicate urbanization boundaries as of
445 2010 (Houston-Galveston Area Council, H-GAC; https://www.h-gac.com/Home) and light grey show location of
446 major intraurban highways. ). Wind vectors are plotted only every 6 grid points to avoid cluttering.

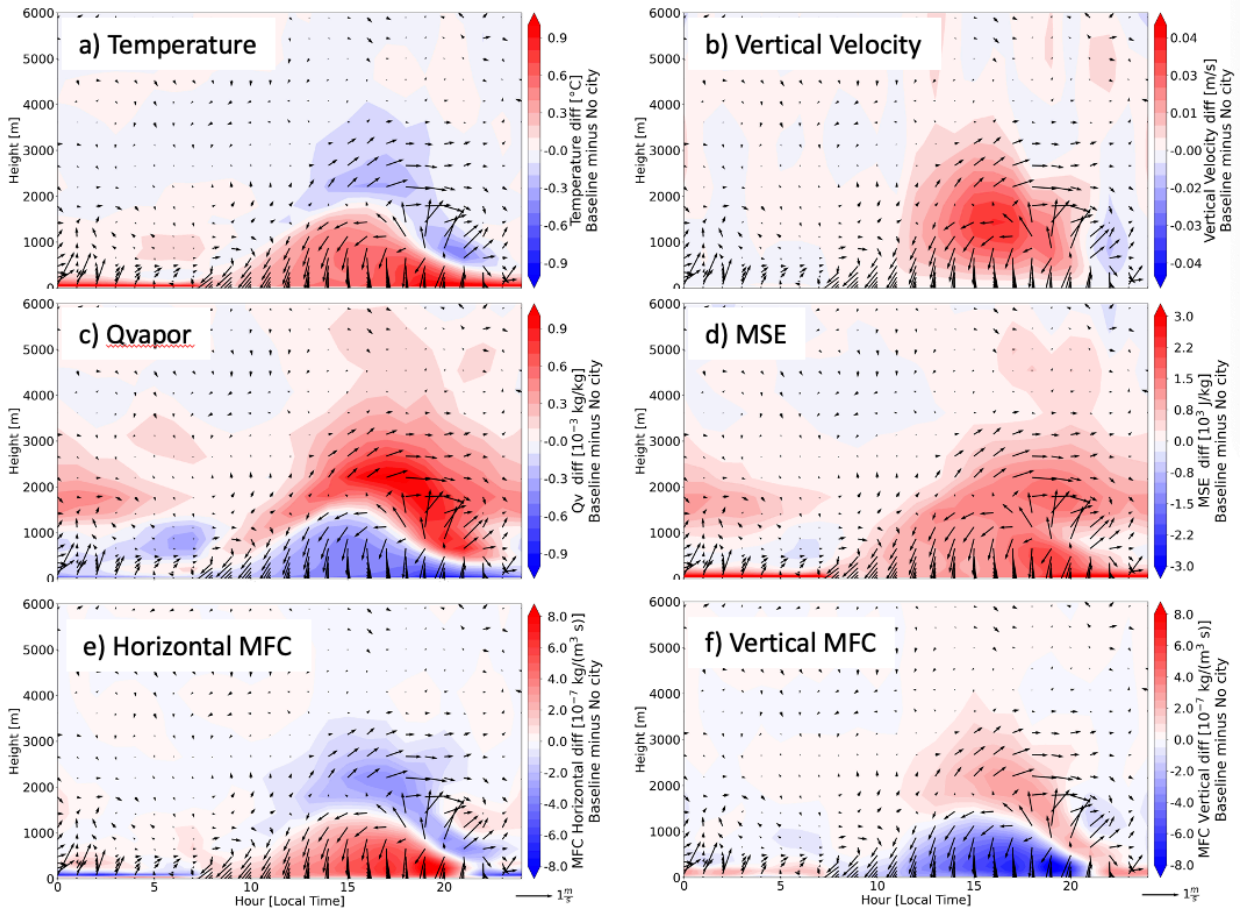


**Figure 11.** Diurnal-height Baseline minus No City scencario differences spatially averaged over the urban areas for (a) air temperature, (b) vertical wind component, (c) water vapor mixing ratio, (d) moist static energy (MSE), (e), horizontal moisture flux convergence, and (f) vertical moisture flux convergence. Vectors in each panel correspond to the horizontal wind, with the north direction pointing upwards. In the vertical, wind vectors are plotted only every 6 grid points to avoid cluttering. MSE = $C_p.T + g.z + L_v.q$, where $C_p$ is the specific heat at constant pressure, T is the air temperature, g is the gravitational constant, z is the geopotential height above MSL, $L_v$ is the laten heat of vaporization, and q is the specific humidity.

It is possible that shallow cumuli and enhanced precipitation (not shown) moisten the cloud and subcloud layers, further favoring more cloud development. Fig. 12 displays a bulk mixing line analysis with the thermodynamical structure of conserved variables (potential temperature and water vapor mixing ratio) in the subcloud and surface layers. The enhanced frequency in entrainment and downdrafts zones in the Baseline relative to the No City simulation further suggest more active cloud dynamics. Notably, when compared to the No City simulation,

461 the Baseline simulation shows that surface fluxes predominantly provide a warmer and dryer
462 mixing lines, with enhanced downdrafts moistening and cooling the subcloud layer. The
463 enhanced cloud downdrafts help explain the layer of relatively cool air above the urban heat
464 island dome shown earlier (Fig. 11a). Furthermore, the Baseline simulation also shows more air
465 masses with warming and drying turbulent entrainment from the free atmosphere into the
466 subcloud layer. Thermodynamically, the enhanced MSE in the subcloud layer (Fig. 11d) is then
467 predominantly maintained by enhanced enthalpy from the surface zone, and partly enhanced by
468 evaporation of the downdrafts and turbulent entrainment. A MSE budget can reveal the
469 proportion of MSE fluxes from each zone, but we refrained to further diagnose the zone
470 contribution fraction because by construction, the non-local closure PBL scheme used in our
471 modeling setup limits a detailed characterization of the mixing lines within the mixed and
472 subcloud layers.

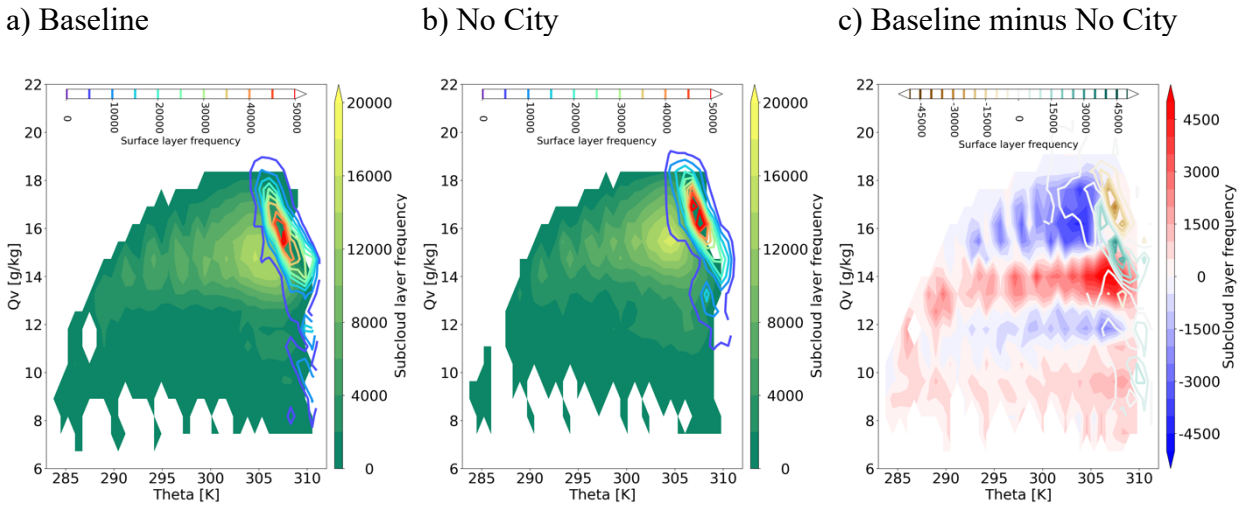


473 **Figure 12.** Mixing line potential temperature and water vapor mixing ratio frequency distribution analyses for
474 (shaded contours) subcloud and (contour) surface layers over the urban area for (a) Baseline, (b) No City, and (c)
475 Baseline minus No City. Only urban grid points in the 12 to 16 LT period were considered.

## 3.4 Sea-Breeze and Urban Induced Circulations

To test the sensitivity of the urban clouds against regional sources of moisture and mesoscale circulations related to the land-sea contrast, we compared the Baseline with the Biased SST simulations. Fig. 13 shows that the warm SSTs adjustment in the Baseline simulation favors more shallow cumulus clouds. The effect of urbanization, however, is still dominant when compared to the warm SSTs adjustment. Notwithstanding is that the warm SSTs adjustment also increases clouds over the rural areas (not shown). By construction, the warmer SSTs develop a warmer low-level atmosphere, with increased latent heat fluxes and water vapor, that in turn, are advected by the predominant southerly and southeasterly flow (Figs. 3, 10). Fig. 14 shows evidence of warming and moistening over the city, with some striking asymmetries in relation to the changes in local circulation and the clouds themselves. The increased water vapor and temperature are related to the more intense MSE signal, which favors a thermodynamical pathway for the enhancement of clouds due to a more unstable lower troposphere, with an enhanced, but weaker relative to the Baseline minus No City, horizontal MFC support. Notably, the urban area shows a low-level cooling and moistening signal concurrent with the enhanced clouds, further displaying the role of the urban clouds and subcloud layer processes in the daytime UHI effect.

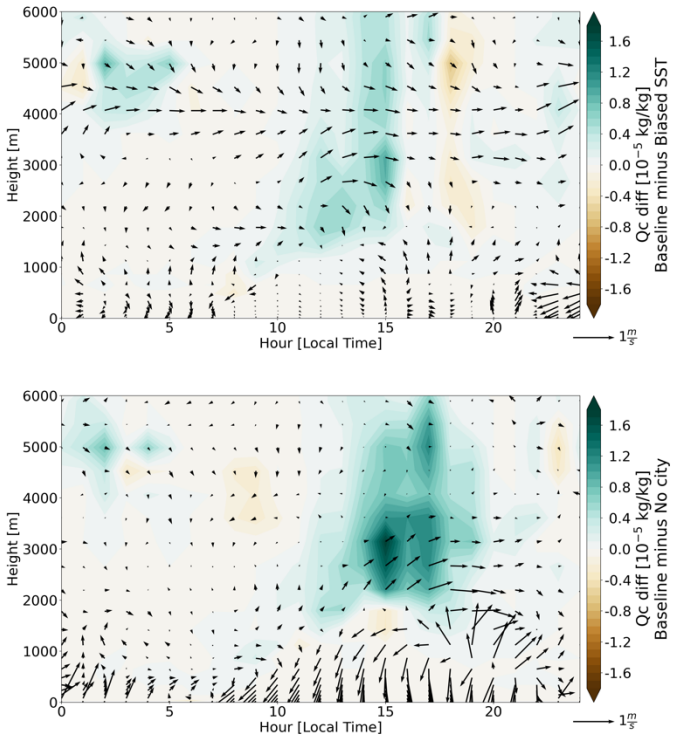


**Figure 13.** Diurnal-height Cloud mixing ratio and wind vector differences spatially averaged over the urban areas for (top panel) Baseline minus Biased SST and (bottom panel) Baseline minus No City. Vectors in each panel correspond to the horizontal wind, with the north direction pointing upwards).

To better display the impact of the No City and Biased SSTs in the mesoscale circulations, Figs. 15 and 16 show 6-hour averaged diurnal time slices for both interpolated fields at 500 m height and latitude-height slices across the city (Fig. 1c). The Baseline minus No City differences show that the urban circulation dome is emphasized as the warm blob collocated with the northerly wind differences. Earlier results showed that this urban circulation dome is favored by the enhanced sensible heat flux, increasing the urban-rural thermal gradient and vertical mixing over the city, and the dynamic frictional drag. Of note is that urbanization imposes anticyclonic and cyclonic differences to the west and east of the city core, respectively, with a horizontal scale as large as the urbanization scale and extending vertically as high as 3500 m above MSL (Fig. 15; Fan et al. 2017). The urban circulation dome seems to dominate the

508 circulation difference, obscuring impacts on the bay- and sea-breeze circulation that have been
509 reported in the literature (Ryu et al. 2016; Shen et al. 2018; Fan et al. 2020; Wang et al. 2023).
510 The impact of warmer SSTs in the Baseline simulation shows an enhancement of the
511 evening-to-morning land-breeze and a weaker sea-breeze (Fig. 15), which agrees with previous
512 SST sensitivity studies (Ryu et al. 2016; Chen et al. 2011). Characterizing the timing and
513 intensity of the sea breeze in the Houston-Galveston area is complicated by the costal shapes and
514 SST differences with a relatively warmer Galveston Bay as compared to the Gulf of Mexico
515 (Salas-Monreal et al. 2018). However, Fig. 16 shows that the weaker sea breeze cell favors the
516 weaker moisture transport near the surface and augments the southerly-southeasterly flow in the
517 return branch of the cell, which help describe the moist difference over the urban area (Fig. 14c).
518 Additionally, the enhanced offshore sensible and latent heat fluxes in the Baseline simulation
519 help develop a deeper and moister marine boundary layer (not shown), further enhancing the
520 transport of water vapor by the background wind and in the return branch of the sea-breeze.

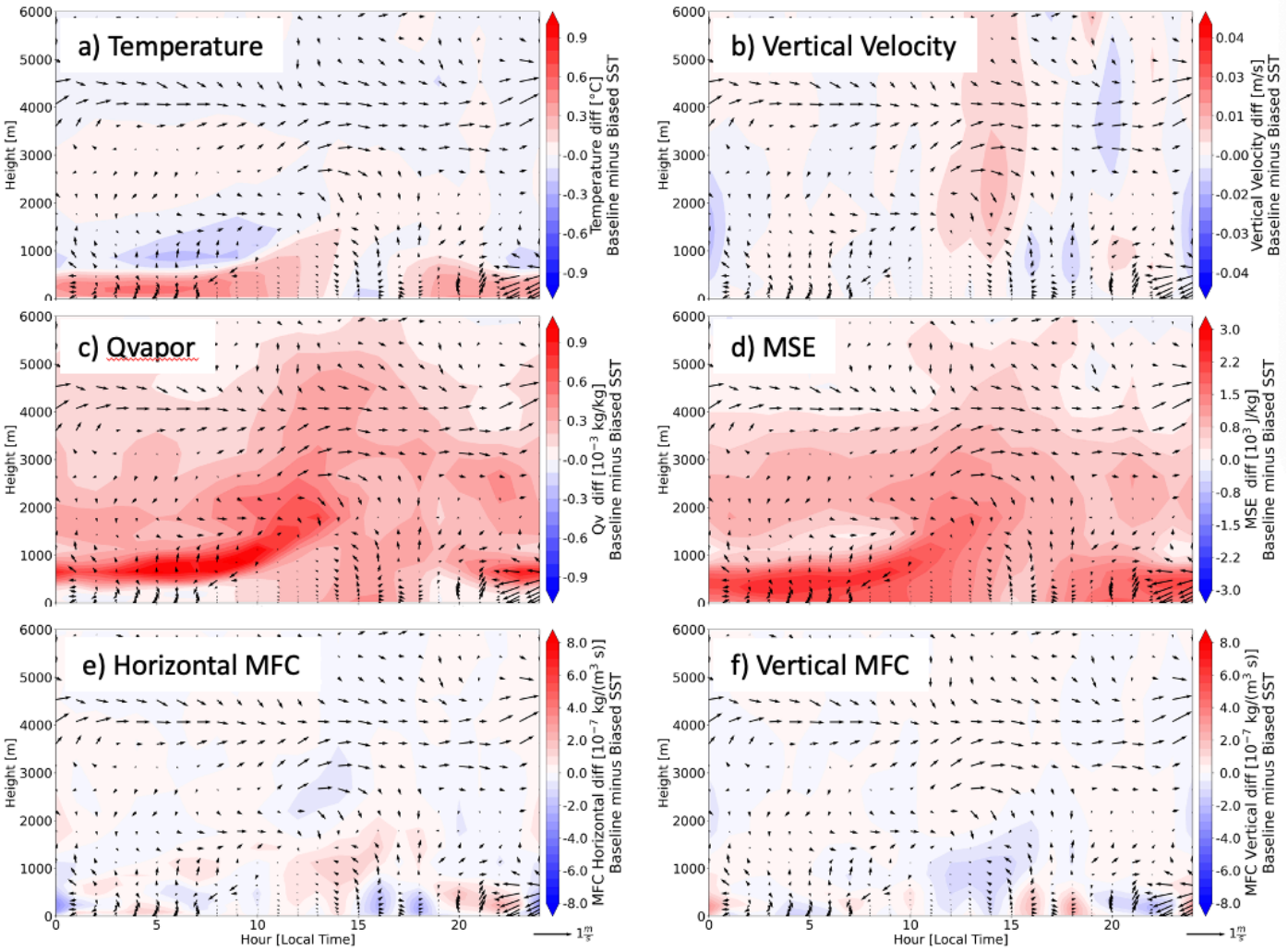


**Figure 14.** Same as Fig. 11 but for Baseline minus Biased SST scencario differences. Vectors in each panel correspond to the horizontal wind, with the north direction pointing upwards. Wind vectors are plotted only every 6 grid point to avoid cluttering.

## 3.5 Heat Index Sensitivity

Here, we examine the role of urbanization, clouds, and SST uncertainties in the Heat Index. Fig. 2 indicated that the model has some limitations in simulating the amplitude of the diurnal cycle of the HI over both rural and urban areas, overemphasizing the HI during the nighttime and underemphasizing the HI during the daytime. Although these diurnal biases can be traced to a low performance in simulating relative humidity, more work is needed to assess the model limitations and sources of uncertainty in stimating the HI. By contrasting the model

532 simulation scenarios, however, we can partly cancel these biases (i.e., linearizing the potential
533 effect of internal feedbacks) and retain the signal related to urbanization, clouds and SST in the
534 diurnal evolution of the HI.

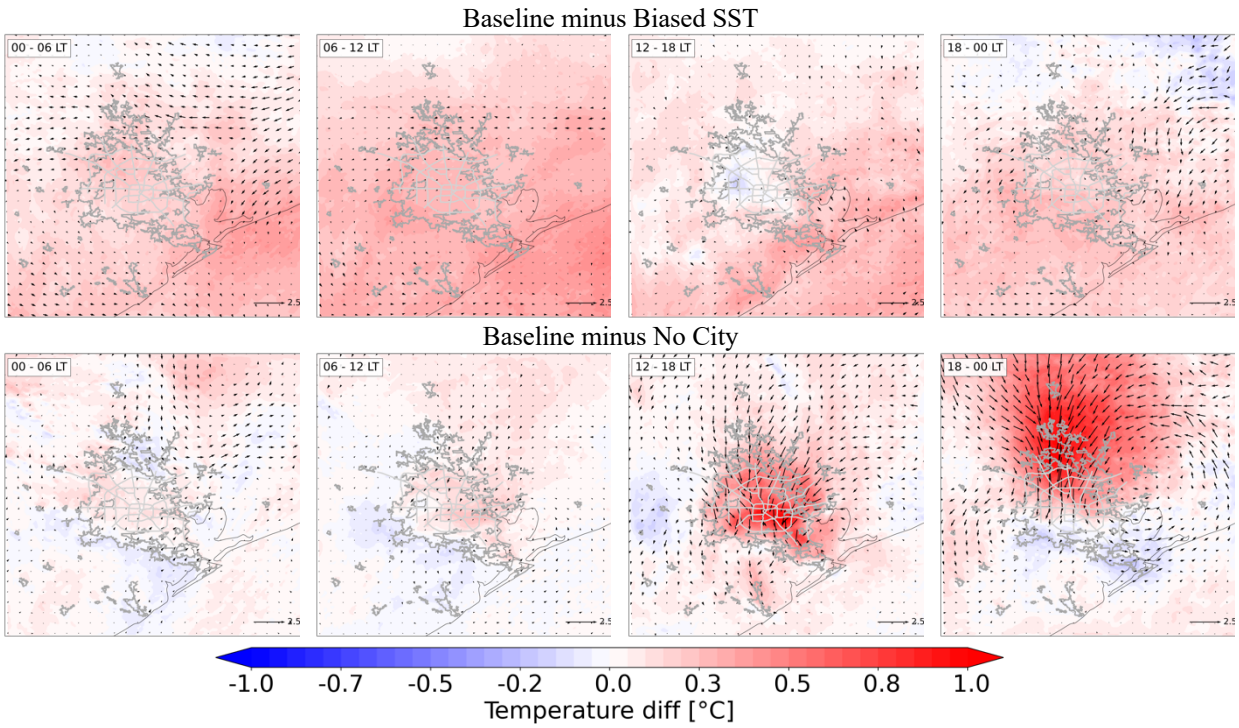


535 **Figure 15.** 500 m (above MSL) height air temperature (contours) and horizontal circulation (vectors) for (top
536 panels) Baseline minus Biased SSTs and (bottom panels) Baseline minus No City differences, diurnally averaged
537 over 6-hour time slices (upper left corner in each panel; Local Time). Wind vectors are plotted every 10 grid point to
538 avoid cluttering. Dark grey contours indicate urbanization boundaries as of 2010 (Houston-Galveston Area Council,
539 H-GAC; https://www.h-gac.com/Home) and light grey show location of major intraurban highways.

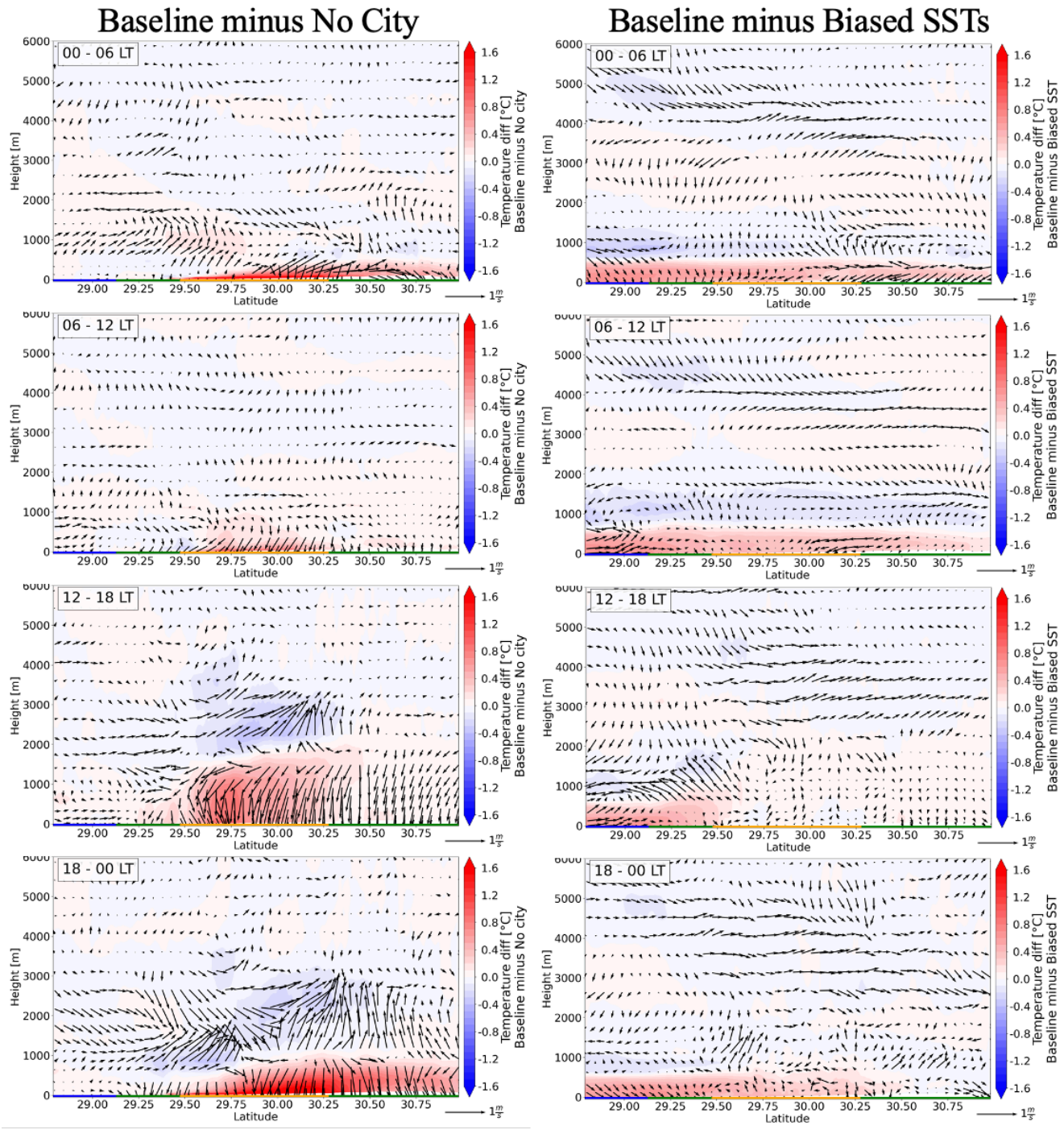


**Figure 16.** Diurnal evolution (top to bottom) of latitude-height temperature and wind vectors for Baseline minus No City and Baseline minus Bias SST analyses along transect displayed in Fig. 1, with colored lines at the bottom of the panels indicating the location of water (blue line), rural (green lines) and urban areas (orange line). Vectors in each panel correspond to the horizontal wind, with the north direction pointing upwards.

546 Figure 17 shows the sensitivity of the HI to urbanization and SST adjustments. On the
547 mean, the UHI has a significant influence in increasing the HI, mostly during the nighttime and
548 early morning. During high HI times (around 15 LT), however, urbanization is related to weaker
549 HI compared to the rural areas, due to the competing impacts of air temperature and relative
550 humidity on the HI. Over the city, the weaker high HI is partly due to the urban dry island effect
551 (Fig. 5c), and partly due to enhanced clouds and its surface cooling effect (Fig 8), limiting high
552 temperatures in the city (Fig. 6). The sensitivity of the HI to moisture is also shown when
553 contrasting Baseline with the Biased SST simulation. Fig. 17 also shows that the warmer SSTs
554 (~1°C) impact the mean HI with a more intense effect near the coast and over the urbanized
555 areas. During high HI, the HI impact of the warmer SSTs over the urban area is less apparent,
556 likely due to the cloud surface cooling effect balancing the warmer and moist sea breeze (Fig.
557 14).

## 558 4 Discussion and Conclusion

559 To better understand the effect of urbanization in meteorology over the Houston-
560 Galveston area, this study developed 900 m grid size simulations between 1-16 August 2020
561 using a cloud- and urban-resolving atmospheric model that includes a Building Energy Model
562 coupled with Building Effect Parameterization. The study investigates the intricate interplay of
563 clouds in local weather, considering various influencing factors. Several model realizations were
564 developed to isolate the role of the urban environment and to address SST biases in the complex
565 Galveston Bay and Gulf of Mexico coast and its effect in the land-sea circulations known to
566 affect the urban climate (Chen at al. 2011; Ngan et al. 2013; Fan et al. 2020). By excluding local
567 anthropogenic aerosols and their effects, this research provides deeper insights into the

relationship between the city and shallow cumulus clouds. These insights contribute to our understanding of the processes modulating excessive heat indicators over urban environments.

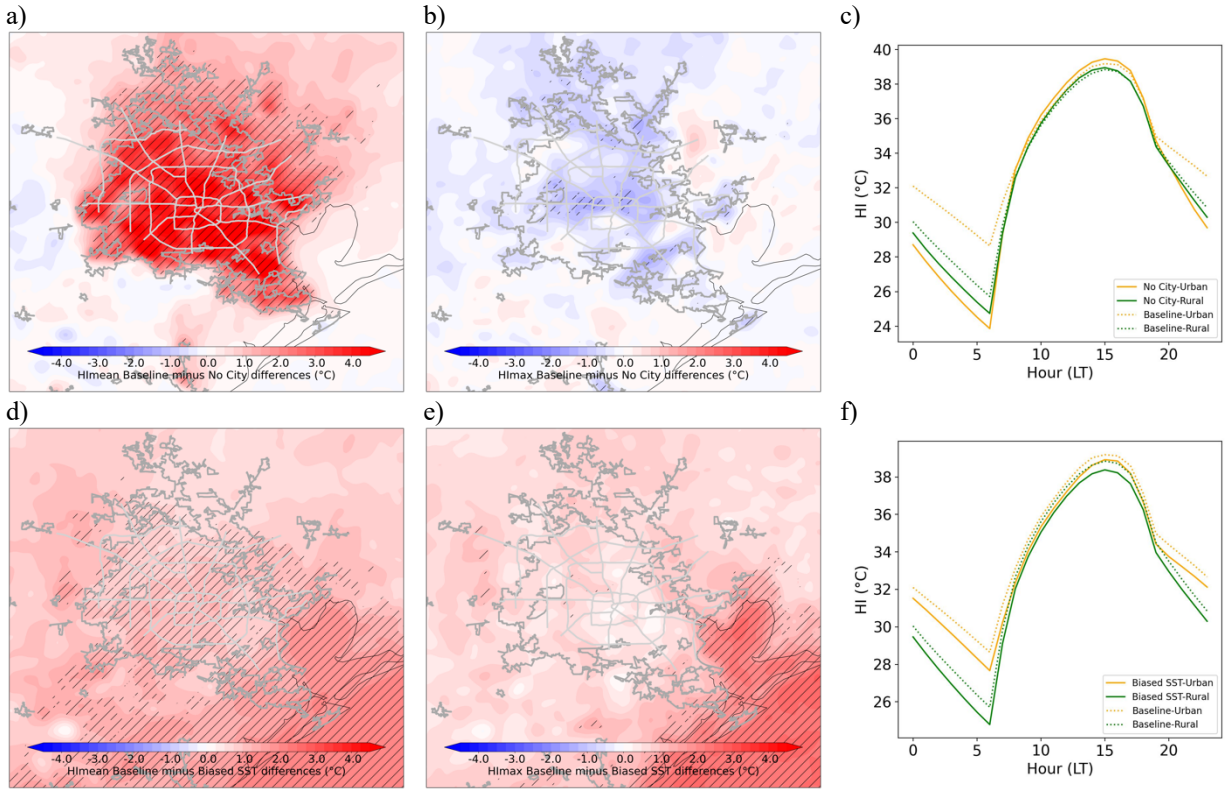


**Figure 17.** *Diurnal mean and maximum Heat Index (HI) differences for Baseline minus No City (a, b, respectively) and Baseline minus Biased SST (d and e, respectively). Hatched areas indicate that differences are significant with a 95% confidence level; Dark grey contours indicate urbanization boundaries as of 2010 (Houston-Galveston Area Council, H-GAC; https://www.h-gac.com/Home) and light grey show location of major intraurban highways. HI diurnal variability composited by rural and urban areas is also added for (c) Baseline and No City and (f) Baseline and Biased SST.*

Through comprehensive model evaluation using 150 surface station sites, an upper-air wind profiler and a cloud climatology, our analyses reveal that the model simulations perform adequately, but common and well-documented biases remained. In agreement with Ngan et al. (2013), the model overestimates southerly winds by overemphasizing the nighttime low-level jet. However, the model also simulates a stronger sea breeze, which is somehow consistent with the urban warm surface temperature bias (Fig. 2), and in turn can favor a more intense temperature gradient during the late evening and early morning and maintaining the onshore see-breeze flow

much longer. Likewise, the warm nighttime temperature bias could be partly related to the outlined biased low-level southerly winds by favoring a larger temperature advection from the offshore waters into land and the urban areas. All results and conclusions relying on advection of environmental parameters, including air pollution constituents (Ngan et al. 2013), into or downstream the city need to be assessed with caution. For example, the downstream extend of the UHI impact to the north and northeast of the city may be overemphasized in this model results due to the strong wind bias. Over rural areas, the warm and dry bias could be related to over advection of the UHI and urban dry island effects (Qian et al. 2022; Fig. 4). The bias differences between the urbanized (Baseline) and the No City simulations show that the city is modulating the surface temperature errors, even over the rural areas (UHI advection and UHI dome and related circulations). On the other hand, Fig. 3d shows that the model simulates a weaker sea-breeze at La Porte when compared to the No City scenario. Previous studies suggest that the enhanced drag imposed by the city decelerates the flow (Chen et al. 2011; Salamanca et al. 2011; Barlow 2014), which we showed reduces the impact of the enhanced thermal driven land-sea circulation due to the warmer city (Fig. 10 and Fig. 15).

It has been suggested that the UHI is more pronounced during the nighttime (Oke 1982), but recent studies have found asymmetries in the time of the maximum diurnal UHI effect, arguing that vegetation type, urban and rural activities (Peng et al. 2012), or clouds (Vo et al. 2023) can affect the time of its maximum. Surface station estimates suggest that during the period of study, the UHI was more intense during the afternoon than during the morning, whereas the model suggested the opposite when evaluated at the same surface station locations. This UHI intensity disagreement is common when comparing surface station observations with urban canopy model output (Hu et al. 2019; Venter et al. 2021; Qian et al. 2022). However,

606 estimating the magnitude of the UHI based on surface station observations is a challenging task,
607 including observational uncertainty issues related to limitations of urban stations in following
608 footprint standards (WMO 2008). Moreover, we noted that the magnitude of the UHI is more
609 pronounced farther from the coast, but also varies according to the location of the rural stations
610 relative to the predominant low-level flow, due to the outlined advection of heat downstream
611 from the city. Our results show the typical ground heat flux driving the nighttime UHI, but other
612 meteorological factors became apparent when considering the interaction with mesoscale
613 circulations and clouds. During the afternoon, we speculate that the smaller simulated diurnal
614 UHI can include possibly the overdoing of the urban clouds, limiting temperature highs in the
615 afternoon, asymmetries in the biases between urban and rural sites, among other model
616 deficiencies. During the nighttime, urbanization enhanced uplift water vapor and clouds slow
617 down the nighttime longwave radiation cooling.

618 Houston-Galveston urbanization favors more shallow cumulus clouds. Our modeling and
619 satellite results support Vo et al. (2023) by showing an apparent cloud enhancement due to
620 urbanization. The simulation period for this study coincides with the time of the year when the
621 urbanization cloud patterns are the largest for Gulf Coast coastal cities (Vo et al. 2023). These
622 results agree with Loughner et al. (2011) and Theeuwes et al. (2019) hypothesis that even over
623 urban areas with relatively drier environments, the surface-driven turbulence can sustain longer-
624 lasting clouds compared to the surrounding rural areas. Despite the model uncertainties and
625 biases shown and discussed above, and without considering the role of aerosols, which play a
626 crucial role in the cloud and precipitation invigoration (Fan et al. 2020) in urban environments,
627 our results help understand the mechanistic processes involved in the urban cloud enhancement.
628 Particularly, our simulations confirm the control of the UHI in the clouds by enhanced vertical

mixing due to aerodynamical drag and an enhanced sensible heat as compared to the surrounding rural areas. In addition, our results also offer a deeper insight on the dynamical and thermodynamical factors interplaying in the cloud enhancement. The city sustains more clouds, with higher cloud heights and deeper shallow cumulus owing to enhanced moist static energy, partly due to enhanced enthalpy by the surface sensible heat and partly due to the enhanced latent heating favored by a stronger low-level horizontal moisture flux convergence (Loughner et al. 2011; Fan et al. 2017; Theeuwes et al. 2022; Chiu et al. 2022). We showed that more clouds, in turn, are related to a cooler surface temperature maximum, when compared to the No City environment and the surrounding rural areas. This cooling can further reduce the afternoon urban-rural heating contrasts and suppress vertical mixing. However, our mixing line analysis also shows that part of this cooling can also be attributed to evaporative cooling downdraft fluxes. Notwithstanding, enhanced MSE is predominantly maintained by the surface heat fluxes, with a minor role from the warm air entrainment fluxes. All these mechanisms also help understand the precipitation enhancement associated with urbanization (SFig. 4; Ryu et al. 2016; Zhu et al., 2016; Lorenz et al. 2019; Statkewicz et al. 2021; Fan et al. 2020, Chiu et al. 2022; Wang et al. 2023) and aerosol-cloud interaction and air pollution impacts (Loughner et al. 2011; Seigel 2014; Fan et al. 2020; Zhong et al. 2015, 2017; Caicedo et al. 2019), which are ongoing observational and modeling research foci (Jensen et al. 2022).

For the first time, our results suggest that the enhanced drag, sensible heat, and vertical mixing related to urbanization act as an obstacle to the prevailing flow, favoring urban circulation dome patterns with a horizontal scale of influence as large as the urban area. Previous studies have suggested that the UHI circulation can strengthen the sea breeze circulation, which favors moisture flux convergence and cooler airflow into the urban environment (Ryu et al.

2016; Zhong et al. 2017; Shen et al. 2018; Fan et al. 2020). However, our results show that dynamical frictional drag due to urbanization slows down the low-level flow with a scale of influence that appears to weaken the thermal-driven bay- and sea-breezes influencing the city. It is possible that deceleration from the urban dynamical drag effect becomes less prominent, and the urban land effect on the sea breeze circulation can become more evident, during weaker or different south-southwesterly background flow regimes (Chen et al. 2011; Ngan et al. 2013; Wang et al. 2022).

Urbanization increases the mean HI, the maximum HI is less intense in the urban area of the Baseline, due to the cloud enhancement pathway as a cooling mechanism. Additionally, the model sensitivities to SSTs revealed that the coastal environment can modulate the UHI intensity, with warmer SSTs producing cooler urban surface temperature highs due to a similar enhanced shallow cumulus cloud pathway, despite the weaker but warmer and moist sea-breeze. Near the coast, the effect of the warmer and more humid environment (due to the warmer SSTs) advected by the sea-breeze appears to have a net intensification of the urban HI, but the maximum HI does not show significant sensitivity, likely due to the competing factors between the surface temperature and relative humidity. These results offer new insights and complement other studies focusing on urbanization and related modulation of the sea breeze as driving mechanisms of the urban heat stress and pollution transport problems in cities near large surface water bodies (Shen et al. 2018; Caicedo et al. 2019; Wang et al. 2023).

Modeling work aiming to assess the impact of heat adaptation and mitigation strategies need to assess the tradeoffs in the UHI circulations and clouds pathways relationships. Most mesoscale urban heat mitigation modeling studies suggest different cooling strategies influencing city scale net cooling effects ranging from ~0.1 to a few degrees °C, depending on the intensity

675 of the implementation (Krayenhoff et al. 2021), but often assume that model biases and other
676 errors are somehow steady under different model conditions and disregard the effect of model
677 errors on relevant physical process. Hence, the impact of cooling strategies can be overwhelmed
678 by uncertainties in SST fields (i.e., those related to observations and data assimilation
679 uncertainties), or by the accuracy of the simulated clouds and precipitation, which is typically an
680 important source of uncertainty in the model.
681
682 *Acknowledgement: This work was funded by NOAA-Climate Program Office Extreme Heat Risk*
683 *Initiative grant number NA21OAR4310149. City of Houston - Mayor's* Office *of Resilience and*
684 Sustainability *and National Weather Service Forecast Office (Timothy Cady), Houston-*
685 *Galveston, TX for their support in this study. High-performance computing was partially*
686 *provided the University of Nevada's Office of Information Technology, Research & Innovation,*
687 *and the Nevada Governor's Office for Economic Development. We extend out thanks to Drs.*
688 *Zonato Andrea and Alberto Martilli for their insight in numerical diffusion issues in earlier*
689 *versions of our model configurations.*
690

691 ## Open Research

692 **Surface Station Data**: All the observational data needed to develop this study is readily
693 available online. This research utilized weather observations from NWS, RAWS, TCEQ, CAMS
694 networks and were obtained using the Synoptic Data PBC Mesonet API (free access to the data
695 via https://mesowest.utah.edu/); buoy implemented is readily accessible in the NOAA data portal
696 (https://www.ndbc.noaa.gov/).

**Wind Profiler Data**: The Cooperative Agency Profilers dataset can be accessed online using NOAA data portal https://madis-data.ncep.noaa.gov/cap/ (last access, 04/02/2024).

**The Model**: The Weather and Research Forecasting model (WRF) is freely available and maintained by the UCAR/National Center for Atmospheric Research (https://www2.mmm.ucar.edu/wrf/users/download/get_source.html) with source version control in the Github portal (https://github.com/wrf-model/WRF/releases).

**World Urban Database and Access Portal (WUDAPT; https://www.wudapt.org/)**: Urban Land Cover/Land Use data used in this study were obtained and distributed by Demuzere et al. (2022) and postprocessing code were made available by Brousse et al. (2016).

**Sea Surface Temperature (SST) Data**: SST used is based on the Advanced Very High Resolution Radiometer (AVHRR) on the European MetOp satellites, and the Visible Infrared Imaging Radiometer Suite (VIIRS) on the U.S. SNPP and NOAA JPSS satellites NOAA-SNPP VIIRS and readily available online (https://eastcoast.coastwatch.noaa.gov/cw_data_access.php).

**Initial and Boundary Conditions**: The Global Tropospheric Analyses and Forecast Grids a (GDAS/FNL; 0.25 degree) were used as initial and boundary conditions to drive the WRF model and is readily accessible online (https://rda.ucar.edu/datasets/ds083.3/; DOI: 10.5065/D65Q4T4Z).

## References

Ancell, B. C., A. Bogusz, M. J. Lauridsen, and C. J. Nauert (2018), Seeding Chaos: The Dire Consequences of Numerical Noise in NWP Perturbation Experiments. *Bull. Amer. Meteor. Soc.*, 99, 615–628, https://doi.org/10.1175/BAMS-D-17-0129.1.

Barlow J.F. (2014), Progress in observing and modelling the urban boundary layer. Urban Clim, 10, https://doi.org/10.1016/j.uclim.2014.03.011

721 Blackadar, A. K. (1957), Boundary layer wind maxima and their significance for the growth of nocturnal
722 inversions. *Bull. Amer. Meteor. Soc.*, 38, 283– 290.
723 Brenguier, J., Pawlowska, H., Schüller, L., Preusker, R., Fischer, J., and Fouquart, Y. (2000), Radiative
724 Properties of Boundary Layer Clouds: Droplet Effective Radius versus Number Concentration,
725 *Journal of the Atmospheric Sciences*, 57(6), 803-821.
726 https://journals.ametsoc.org/view/journals/atsc/57/6/1520-
727 0469_2000_057_0803_rpoblc_2.0.co_2.xml
728 Bouali, M., and A. Ignatov (2014), Adaptive Reduction of Striping for Improved Sea Surface
729 Temperature Imagery from Suomi National Polar-Orbiting Partnership (S-NPP) Visible Infrared
730 Imaging Radiometer Suite (VIIRS). *J. Atmos. Oceanic Technol.*, 31, 150–
731 163, https://doi.org/10.1175/JTECH-D-13-00035.1.
732 Brousse Oscar, Alberto Martilli, Michael Foley, Gerald Mills, Benjamin Bechtel (2016), WUDAPT, an
733 efficient land use producing data tool for mesoscale models? Integration of urban LCZ in WRF over
734 Madrid, *Urban Climate*, 17, 116-134, https://doi.org/10.1016/j.uclim.2016.04.001.
735 Cady, T. J., Rahn, D. A., Brunsell, N. A., & Lyles, W. (2020), Conversion of Abandoned Property to
736 Green Space as a Strategy to Mitigate the UHI Investigated with Numerical Simulations, *J. Appl.*
737 *Meteor. Climatol.*, 59(11), 1827-1843. https://doi.org/10.1175/JAMC-D-20-0093.1
738 Caicedo, V., et al. (2019), Bay breeze and sea breeze circulation impacts on the planetary boundary layer
739 and air quality from an observed and modeled DISCOVER-AQ TX case study. *Journal of*
740 *Geophysical Research: Atmospheres*, 124, 7359–7378. https://doi.org/10.1029/2019JD030523
741 Chen F., Miao S., Tewari M., Bao J.W., Kusaka H (2011), A numerical study of interactions between
742 surface forcing and sea breeze circulations and their effects on stagnation in the greater Houston area.
743 *J. Geophys. Res. Atmos.*;116:1–19. doi: 10.1029/2010JD015533.
744 Ching, J., and Coauthors (2009), National Urban Database and Access Portal Tool. *Bull. Amer. Meteor.*
745 *Soc.*, 90, 1157–1168, https://doi.org/10.1175/2009BAMS2675.1.

Ching, J., Mills, G., Bechtel, B., See, L., Feddema, J., Wang, X., … Theeuwes, N. (2018), WUDAPT: An Urban Weather, Climate, and Environmental Modeling Infrastructure for the Anthropocene. *Bull. Amer. Meteor. Soc.*, 99(9), 1907–1924. https://doi.org/10.1175/BAMS-D-16-0236.1

Chiu C.T.F., Kai Wang, Athanasios Paschalis, Tohid Erfani, Nadav Peleg, Simone Fatichi, Natalie Theeuwes, Gabriele Manoli (2022), An analytical approximation of urban heat and dry islands and their impact on convection triggering, *Urban Climate*, 46, https://doi.org/10.1016/j.uclim.2022.101346.

Crosman, Erik T. and Horel, John D. (2012), Idealized Large-Eddy Simulations of Sea and Lake Breezes: Sensitivity to Lake Diameter, Heat Flux and Stability, *Boundary-Layer Meteorology*, 144(3), 309–328, https://doi.org/10.1007/s10546-012-9721-x

Demuzere M, Kittner J, Bechtel B. (2021), LCZ Generator: A Web Application to Create Local Climate Zone Maps. *Front Environ Sci*.;9. doi:10.3389/fenvs.2021.637455.

Demuzere, M., Kittner, J., Martilli, A., Mills, G., Moede, C., Stewart, I. D., van Vliet, J., and Bechtel, B. (2022a), A global map of Local Climate Zones to support earth system modelling and urban scale environmental science, *Earth Syst. Sci. Data* 14(8) 3835-3873. DOI: 10.5194/essd-14-3835-2022.

Demuzere M, Argüeso D, Zonato A, Kittner J. (2022b) W2W: A Python package that injects WUDAPT's Local Climate Zone information in WRF. J Open Source Softw. 2022a;7(76):4432. Doi:10.21105/joss.04432.

Demuzere M, He C, Martilli A, Zonato A (2023). A hybrid 100-m global land cover dataset with Local Climate Zones for WRF. [Data set]. Zenodo. https://doi.org/10.5281/zenodo.7670653

Doan, Q., S. Kobayashi, H. Kusaka, F. Chen, C. He, and D. Niyogi (2023), Tracking Urban Footprint on Extreme Precipitation in an African Megacity. *J. Appl. Meteor. Climatol.*, 62, 209–226, https://doi.org/10.1175/JAMC-D-22-0048.1.

Ebi, K. L., Capon, A., Berry, P., Broderick, C., de Dear, R., Havenith, G., ... & Jay, O. (2021), Hot weather and heat extremes: health risks. *The Lancet*, 398(10301), 698-708.

771 Fan, J., Zhang, Y., Li, Z., Hu, J., and Rosenfeld, D. (2020), Urbanization-induced land and aerosol
772 impacts on sea-breeze circulation and convective precipitation, *Atmos. Chem. Phys.*, 20, 14163–
773 14182, https://doi.org/10.5194/acp-20-14163-2020.
774 Fan, Y. F., Y. G. Li, A. Bejan, Y. Wang, and X. Y. Yang (2017), Horizontal extent of the urban heat
775 dome flow. *Scientific Reports*, 7, 11681, https://doi.org/10.1038/s41598-017-09917-4.
776 Fischer, E., Schär, C. (2010), Consistent geographical patterns of changes in high-impact European
777 heatwaves. *Nature Geosci,* 3, 398–403, https://doi.org/10.1038/ngeo866
778 Guo Y, Gasparrini A, Li S, Sera F, Vicedo-Cabrera AM, de Sousa Zanotti Stagliorio Coelho M, et al.
779 (2018), Quantifying excess deaths related to heatwaves under climate change scenarios: A
780 multicountry time series modelling study. *PLoS Med* 15(7): e1002629.
781 Hawbecker, P., and J. C. Knievel (2022), Simulating the Chesapeake Bay Breeze: Sensitivities to Water
782 Surface Temperature. *J. Appl. Meteor. Climatol.*, 61, 1595–1611, https://doi.org/10.1175/JAMC-D-
783 22-0002.1.
784 Hendricks, E. A., Knievel, J. C., & Wang, Y. (2020), Addition of Multilayer Urban Canopy Models to a
785 Nonlocal Planetary Boundary Layer Parameterization and Evaluation Using Ideal and Real Cases, *J.*
786 *Appl. Meteor. Climatol.*, 59(8), 1369-1392,
787 https://journals.ametsoc.org/view/journals/apme/59/8/jamcD190142.x
788 Houston Climate Action Plan (2020), http://greenhoustontx.gov/climateactionplan/
789 Hu, Y. H., M. T. Hou, G. S. Jia, C. L. Zhao, X. J. Zhen, and Y. H. Xu (2019), Comparison of surface and
790 canopy urban heat islands within megacities of eastern China. *ISPRS Journal of Photogrammetry and*
791 *Remote Sensing*, 156, 160−168, https://doi.org/10.1016/j.isprsjprs.2019.08.012.
792 Jensen, M. P., Flynn, J. H., Judd, L. M., Kollias, P., Kuang, C., Mcfarquhar, G., Nadkarni, R., Powers, H.,
793 and Sullivan, J. (2022), A succession of cloud, precipitation, aerosol, and air quality field
794 experiments in the coastal urban environment, *Bull. Amer. Meteor. Soc.*, 103(2), 103-105.
795 https://journals.ametsoc.org/view/journals/bams/103/2/BAMS-D-21-0104.1.xml

796 Jin, L., Schubert, S., Fenner, D. et al. (2021), Integration of a Building Energy Model in an Urban
797 Climate Model and its Application. Boundary-Layer Meteorol, 178, 249–281.
798 https://doi.org/10.1007/s10546-020-00569-y
799 Knievel, J. C., Bryan, G. H., & Hacker, J. P. (2007), Explicit Numerical Diffusion in the WRF Model,
800 *Monthly Weather Review*, 135(11), 3808-3824.
801 https://journals.ametsoc.org/view/journals/mwre/135/11/2007mwr2100
802 Krayenhoff, Eric and Broadbent, Ashley & Zhao, Lei & Georgescu, Matei & Middel, Ariane & Voogt,
803 James and Martilli, Alberto & Sailor, David & Erell, Evyatar. (2021), Cooling hot cities: A
804 systematic and critical review of the numerical modelling literature. *Environmental Research Letters*,
805 16, 10.1088/1748-9326/abdcf1.
806 Lorenz, J. M., Kronenberg, R., Bernhofer, C., & Niyogi, D. (2019), Urban rainfall modification:
807 Observational climatology over Berlin, Germany. *Journal of Geophysical Research: Atmospheres*,
808 124, 731–746. https://doi.org/10.1029/2018JD028858
809 Loughner, C. P., D. J. Allen, K. E. Pickering, R. R. Dickerson, D.-L. Zhang, and Y.-X. Shou (2011),
810 Impact of the Chesapeake Bay breeze and fair-weather cumulus clouds on pollutant transport and
811 transformation. *Atmos. Environ.*, 24, 4060–4072.
812 Morris, C. J. G., Simmonds, I., Plummer, N. (2001), Quantification of the Influences of Wind and Cloud
813 on the Nocturnal Urban Heat Island of a Large City. *Journal of Applied Meteorology,* 40(2), 169-18.
814 National Centers for Environmental Prediction/National Weather Service/NOAA/U.S. Department of
815 Commerce. 2015, updated daily. NCEP GDAS/FNL 0.25 Degree Global Tropospheric Analyses and
816 Forecast Grids. Research Data Archive at the National Center for Atmospheric Research,
817 Computational and Information Systems Laboratory. https://doi.org/10.5065/D65Q4T4Z. Last
818 accessed 03 March 2021.
819 Ngan, F., H. Kim, P. Lee, K. Al-Wali, and B. Dornblaser (2013), A Study of Nocturnal Surface Wind
820 Speed Overprediction by the WRF-ARW Model in Southeastern Texas. *J. Appl. Meteor. Climatol.*,
821 52, 2638–2653, https://doi.org/10.1175/JAMC-D-13-060.1.

822 Oke, T. R. (1982), The energetic basis of the urban heat island. *Q. J. R. Meteorolog. Soc.* 108, 1–24.
823 Palecki, Michael; Durre, Imke; Applequist, Scott; Arguez, Anothony; Lawrimore, Jay. 2021: U.S.
824 Climate Normals 2020: U.S. Climate Normals (1991-2020). HOUSTON NWSO, TX (station ID:
825 USC00414333). NOAA National Centers for Environmental Information. Web portal:
826 https://www.ncei.noaa.gov/.
827 Peng, S. et al. (2012), Surface urban heat island across 419 global big cities. *Environ. Sci. Technol.* 46,
828 696–703. https://doi.org/10.1021/es2030438
829 Pu, B., and R. E. Dickinson (2014), Diurnal Spatial Variability of Great Plains Summer Precipitation
830 Related to the Dynamics of the Low-Level Jet. *J. Atmos. Sci.*, 71, 1807–1817,
831 https://doi.org/10.1175/JAS-D-13-0243.1.
832 Qian Y, Chakraborty TC, Li J, Li D, He C, Sarangi C, Chen F, Yang X, Leung LR. (2022), Urbanization
833 Impact on Regional Climate and Extreme Weather: Current Understanding, Uncertainties, and Future
834 Research Directions. *Adv Atmos Sci.* 2022;39(6):819-860. doi: 10.1007/s00376-021-1371-9.
835 Resilient Houston, (2020). https://www.houstontx.gov/mayor/Resilient-Houston-20200518-single-
836 page.pdf
837 Rosenzweig, C., et al. (2014), Enhancing Climate Resilience at NASA Centers: A Collaboration between
838 Science and Stewardship, *Bull. Amer. Meteor. Soc.*, 95(9), 1351-1363,
839 https://journals.ametsoc.org/view/journals/bams/95/9/bams-d-12-00169.1.xml
840 Rothfusz, L. P. (1990), The heat index “equation” (or, more than you ever wanted to know about heat
841 index). NWS Tech. Attachment SR 90-23, 2 pp.
842 Ryu, Y., J. A. Smith, E. Bou-Zeid, and M. L. Baeck (2016), The Influence of Land Surface
843 Heterogeneities on Heavy Convective Rainfall in the Baltimore–Washington Metropolitan Area.
844 *Mon. Wea. Rev.*, 144, 553–573, https://doi.org/10.1175/MWR-D-15-0192.1.
845 Salamanca, F., A. Martilli, M. Tewari, and F. Chen (2011), A Study of the Urban Boundary Layer Using
846 Different Urban Parameterizations and High-Resolution Urban Canopy Parameters with WRF. *J.*
847 *Appl. Meteor. Climatol.*, 50, 1107–1128, https://doi.org/10.1175/2010JAMC2538.1.

Salas-Monreal D., Ayal Anis, David Alberto Salas-de-Leon (2018), Galveston Bay dynamics under different wind conditions, *Oceanologia*, 232-243, https://doi.org/10.1016/j.oceano.2017.10.005.

Schubert S, Grossman-Clarke S, Martilli A. (2012), A double-canyon radiation scheme for multi-layer urban canopy models. *Boundary-Layer Meteorol,* 145(3):439–468

Seigel, R. B. (2014), Shallow Cumulus Mixing and Subcloud-Layer Responses to Variations in Aerosol Loading. *J. Atmos. Sci.*, 71, 2581–2603, https://doi.org/10.1175/JAS-D-13-0352.1.

Shen, L. D., J. N. Sun, and R. M. Yuan (2018), Idealized large eddy simulation study of interaction between urban heat island and sea breeze circulations. *Atmospheric Research,* 214, 338−347, https://doi.org/10.1016/j.atmosres.2018.08.010.

Simolo, C., Brunetti, M., Maugeri, M., and Nanni, T. (2011), Evolution of extreme temperatures in a warming climate, *Geophys. Res. Lett.*, 38, L16701, doi:10.1029/2011GL048437.

Statkewicz M.D., Robert Talbot, Bernhard Rappenglueck (2021), Changes in precipitation patterns in Houston, Texas, *Environmental Advances*, 5, 100073, ISSN 2666-7657, https://doi.org/10.1016/j.envadv.2021.100073.

Statkewicz M.D., B. Rappenglueck (2023), A comparative analysis of the sea breeze on the Texas Gulf Coast and its impact on precipitation, Urban Climate, 49, https://doi.org/10.1016/j.uclim.2023.101568.

Theeuwes N. E., I. A. Boutle, P. A. Clark, S. Grimmond (2021), Understanding London's summertime cloud cover. *Q. J. R. Meteorol. Soc*. 148(742), 454–465. https://doi.org/10.1002/qj.4214

Theeuwes, N.E., Barlow, J.F., Teuling, A.J. *et al.* (2019), Persistent cloud cover over mega-cities linked to surface heat release. *npj Clim Atmos Sci* **2**, 15. https://doi.org/10.1038/s41612-019-0072-x

Trenberth, K., Fasullo, J. & Shepherd, T. (2015), Attribution of climate extreme events. *Nature Clim Change* 5, 725–730 https://doi.org/10.1038/nclimate2657

USGCRP (2018), Impacts, Risks, and Adaptation in the United States: Fourth National Climate Assessment*, Volume II* [Reidmiller, D.R., C.W. Avery, D.R. Easterling, K.E. Kunkel, K.L.M. Lewis,

873 T.K. Maycock, and B.C. Stewart (eds.)]. U.S. Global Change Research Program, Washington, DC,
874 USA, 1515 pp. doi: 10.7930/NCA4.2018.
875 Venter, Z. S., T. Chakraborty, and X. Lee (2021), Crowdsourced air temperatures contrast satellite
876 measures of the urban heat island and its mechanisms. *Science Advances*, 7, eabb9569,
877 https://doi.org/10.1126/sciadv.abb9569.
878 Vo, Trang Thuy & Hu, Leiqiu & Xue, Lulin & Li, Qi & Chen, Sisi (2023), Urban effects on local cloud
879 patterns. *Proceedings of the National Academy of Sciences of the United States of America*. 120.
880 e2216765120. 10.1073/pnas.2216765120.
881 Wang, J., Yun Qian, William Pringle, T.C. Chakraborty, Robert Hetland, Zhao Yang, Pengfei Xue
882 (2023), Contrasting effects of lake breeze and urbanization on heat stress in Chicago metropolitan
883 area, *Urban Climate*, 48, https://doi.org/10.1016/j.uclim.2023.101429.
884 Wang, D., Jensen, M. P., Taylor, D., Kowalski, G., Hogan, M., Wittemann, B. M., et al. (2022), Linking
885 synoptic patterns to cloud properties and local circulations over southeastern Texas. *Journal of*
886 *Geophysical Research: Atmospheres*, 127, e2021JD035920. https://doi.org/10.1029/2021JD035920
887 Williams, A. P., Schwartz, R. E., Iacobellis, S., Seager, R., Cook, B. I., Still, C. J., Husak, G. and
888 Michaelsen, J. (2015), Urbanization causes increased cloud base height and decreased fog in coastal
889 Southern California. *Geophys. Res. Lett.*, 42: 1527– 1536. doi: 10.1002/2015GL063266.
890 Wilson AM, Jetz W (2016), Remotely Sensed High-Resolution Global Cloud Dynamics for Predicting
891 Ecosystem and Biodiversity Distributions. *PLoS Biol* 14(3): e1002415. doi:10.1371/journal.
892 pbio.1002415" Data available on-line at http://www.earthenv.org/.
893 WMO (2008), Guide to Meteorological Instruments and Methods of Observation. World Meteorological
894 Organization.
895 Zhong, S., Qian, Y., Zhao, C., Leung, R., and Yang, X. Q. (2015), A case study of urbanization impact on
896 summer precipitation in the Greater Beijing Metropolitan Area: Urban heat island versus aerosol
897 effects, *J. Geophys. Res.-Atmos.*, 120, 10903–10914, https://doi.org/10.1002/2015jd023753.

Zhong, S., Qian, Y., Zhao, C., Leung, R., Wang, H., Yang, B., Fan, J., Yan, H., Yang, X.-Q., and Liu, D. (2017), Urbanization-induced urban heat island and aerosol effects on climate extremes in the Yangtze River Delta region of China, *Atmos. Chem. Phys.*, 17, 5439–5457, https://doi.org/10.5194/acp-17-5439-2017.

Zhu, X., Ni, G., Cong, Z., Sun, T., and Li, D. (2016), Impacts of surface heterogeneity on dry planetary boundary layers in an urban-rural setting, *J. Geophys. Res. Atmos.*, 121, 12,164– 12,179, doi:10.1002/2016JD024982.

Zonato, A., Martilli, A., Gutierrez, E., Chen, F., He, C., Barlage, M., et al. (2021), Exploring the effects of rooftop mitigation strategies on urban temperatures and energy consumption. *Journal of Geophysical Research: Atmospheres*, 126, e2021JD035002. https://doi.org/10.1029/2021JD035002

# Supplemental Material

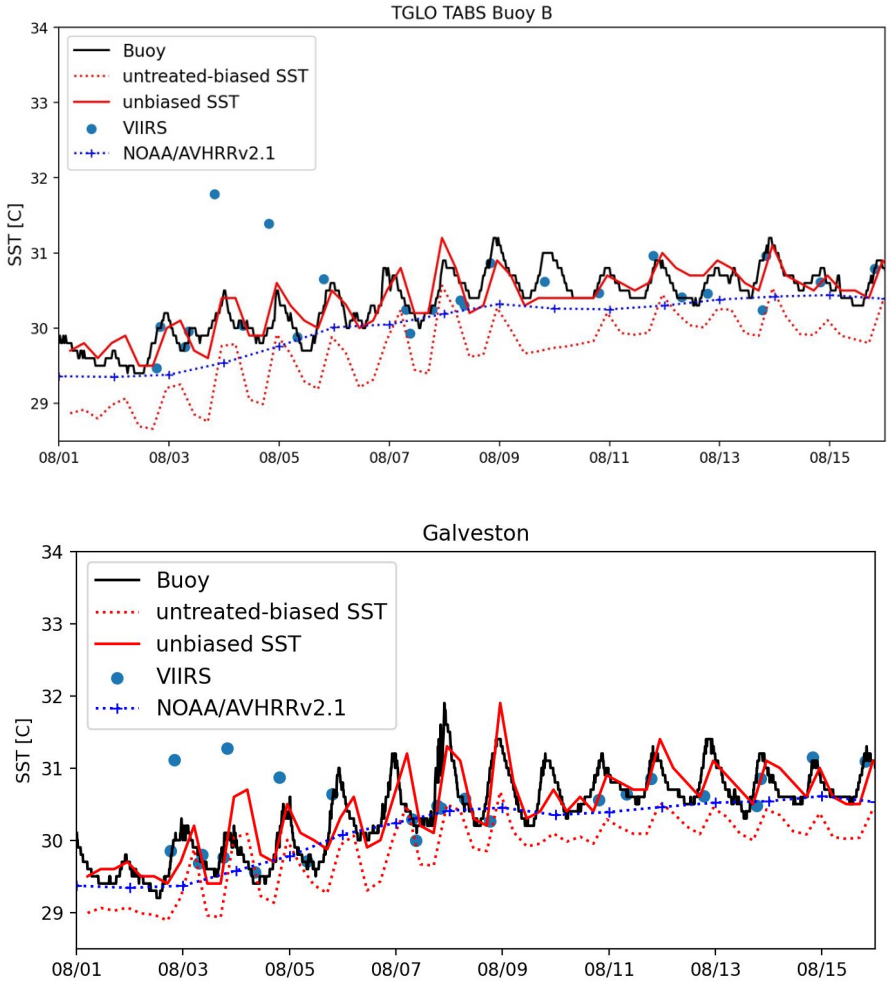


**SFigure 1.** (Top panel) TGLO TABS Buoy B and (bottom panel) Galveston hourly buoy SST, twice a day remotely sensed data (NOAA-SNPP VIIRS SST) and untreated-biased SST (after preprocessed by WRF) and biased-corrected or unbiased SSTs. Date (MM/DD) range for the first half of August 2020.

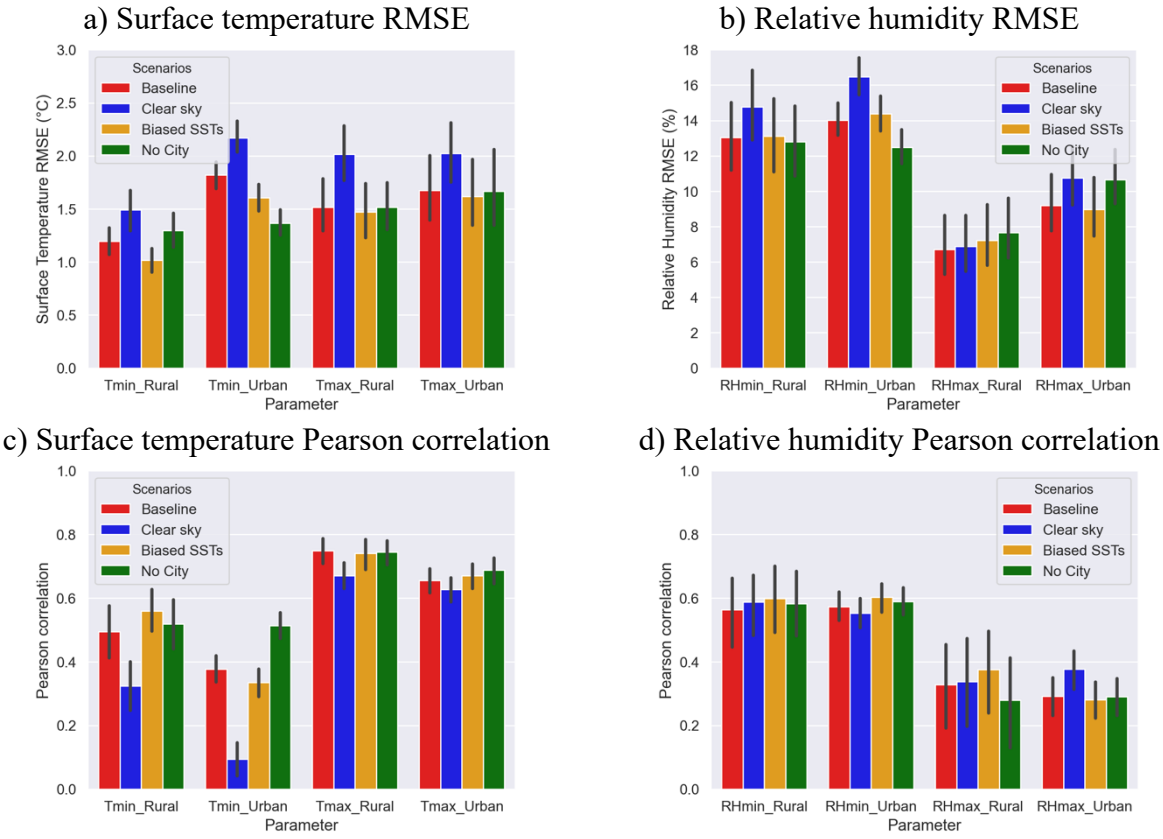


922 **SFigure 2.** Simulated RMSE and Pearson correlation for evaluated at surface station sites for different scenarios
923 (Table 2) for (a, c) daily for surface temperature low and high (Tmin, Tmax), (b, d) relative humidity maximum and
924 minimum (RHmax, RHmin), and corresponding bias distribution for all examined surface station sites as
925 categorized as Urban or Rural according to MODIS/WUDAPTv2 land use/land cover types. Evaluation period is 1-
926 16 August 2020. Analysis constrained to non-rainy periods as described in the text.

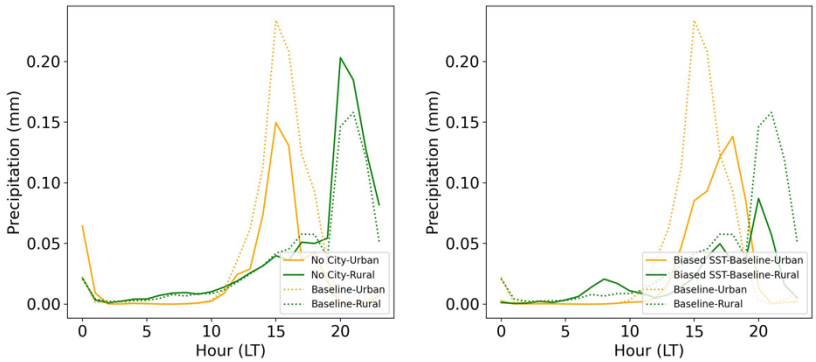


927

928 **SFigure 4.** Spatially averaged diurnal precipitation in the urban and rural areas for (left panel) Baseline and No City
929 and (right panel) Baseline and Biased-SST scenarios.